Cosmology with the redshift-space galaxy bispectrum monopole at one-loop order

Oliver H. E. Philcox,[1,2,*] Mikhail M. Ivanov,[2,†] Giovanni Cabass,[2] Marko Simonović,[3] Matias Zaldarriaga,[2] and Takahiro Nishimichi[4,5]

[1]*Department of Astrophysical Sciences, Princeton University, Princeton, New Jersey 08540, USA*
[2]*School of Natural Sciences, Institute for Advanced Study, 1 Einstein Drive, Princeton, New Jersey 08540, USA*
[3]*Theoretical Physics Department, CERN, 1 Esplanade des Particules, Geneva 23, CH-1211, Switzerland*
[4]*Center for Gravitational Physics and Quantum Information, Yukawa Institute for Theoretical Physics, Kyoto University, Kyoto 606-8502, Japan*
[5]*Kavli Institute for the Physics and Mathematics of the Universe (WPI), UTIAS The University of Tokyo, Kashiwa, Chiba 277-8583, Japan*

(Received 13 June 2022; accepted 8 August 2022; published 23 August 2022)

We study the cosmological information content of the redshift-space galaxy bispectrum monopole at one-loop order in perturbation theory. We incorporate all effects necessary for comparison to data: fourth-order galaxy bias, infrared resummation (accounting for the nonlinear evolution of baryon acoustic oscillations), ultraviolet counterterms, nonlinear redshift-space distortions, stochastic contributions, projection, and binning effects. The model is implemented using FFTLog, and validated with the PT Challenge suite of N-body simulations, whose large volume allows for high-precision tests. Focusing on the mass fluctuation amplitude, σ_8, and galaxy bias parameters, we find that including one-loop corrections allow us to significantly extend the range of scales over which the bispectrum can be modeled, and greatly tightens constraints on bias parameters. However, this does not lead to noticeable improvements in the σ_8 error bar due to the necessary marginalization over a large number of nuisance parameters with conservative priors. Analyzing a BOSS-volume likelihood, we find that the addition of the one-loop bispectrum may lead to improvements on primordial non-Gaussianity constraints by $\lesssim$30% and on σ_8 by $\approx$10%, though we caution that this requires pushing the analysis to short scales where the galaxy bias parameters may not be correctly recovered; this may lead to biases in the recovered parameter values. We conclude that restrictive priors from simulations or higher-order statistics such as the bispectrum multipoles will be needed in order to realize the full information content of the galaxy bispectrum.

DOI: 10.1103/PhysRevD.106.043530

I. INTRODUCTION

The distribution of matter in the Universe is not Gaussian. As such, any optimal analysis of large-scale structure surveys must involve non-Gaussian statistics. Historically, the distribution of galaxies has been analyzed by way of the power spectrum, which is a complete statistic only in the Gaussian (large-scale) limit. Such analyses have seen particular successes, both in measuring the Universe's growth rate and expansion history via baryon acoustic oscillation signatures (e.g., [1–8]), and in the direct determination of cosmological parameters using full-shape methods (e.g., [9–27]). However, if we wish to extract more information from the observational datasets (and thus enhance their utility at fixed experimental cost), we must additionally include higher-order statistics, of which the simplest are the bispectrum and three-point correlation function.

Much as the power spectrum describes the distribution of pairs of points, the bispectrum encodes the statistics of triplets [28]. Despite being a subject of significant early work (e.g., [29–37]), the bispectrum has been rarely used in modern cosmological analyses (though see [38–40]), owing to difficulties in its measurement (cf. [41–43]), modeling, and interpretation. On the other hand, its potential utility has been demonstrated a number of times, with claims of tight constraints on a number of cosmological parameters, particularly those encoding extensions

*ohep2@cantab.ac.uk
†ivanov@ias.edu

to the ΛCDM paradigm, such as neutrino masses, primordial non-Gaussianity and the breaking of the equivalence principle [44–65]. To fully utilize this information, we require theoretical models capable of predicting the shape of the bispectrum and its dependence on the parameters of interest. This has been a subject of significant work, starting from the matter bispectrum [66–73], then incorporating the effects of redshift-space distortions [37,74–76] and galaxy bias [62,77–81], most successfully using the effective field theory (EFT) of large scale structure [82,83] (see [84] for a recent review).

Whilst the above references have been pivotal to the development of a bispectrum model, few contain all the necessary ingredients to allow for robust comparison of theory and observation. In particular, one must account for the backreaction of short-scale physics on the large-scale bispectrum [66,67,85], long-wavelength displacements [86–93], and survey geometry [94,95], all of which can lead to biases in derived parameters if not properly accounted for. In [80] a complete model for the tree-level (leading-order) bispectrum of galaxies in redshift-space was presented and validated, including all the above effects (see also [19]). This allows for precise modeling of the angle-averaged bispectrum monopole, and has facilitated a number of analyses constraining ΛCDM parameters [15] and primordial non-Gaussianity [96,97]. However, this model was restricted to relatively large scales ($k < 0.08\ h^{-1}\,\mathrm{Mpc}$ at $z = 0.61$). If we wish to further exploit the constraining power of the bispectrum, we must push to smaller scales by extending the perturbation theory to next order. Whilst [98] has recently demonstrated some work in this direction, a full model for the one-loop bispectrum (including all relevant phenomena such as projection effects) has not yet been presented and validated with simulations.

In this work, we present a complete and systematic computation of the redshift-space galaxy bispectrum monopole at one-loop order. This includes all effects necessary to compare with observational data: deterministic contributions, counterterms, bias renormalization, stochasticity, bin averaging, and coordinate distortions. This involves the galaxy density at fourth-order: we systematically account for all bias operators (following [79]), and include full treatment of all necessary redshift-space counterterms, ensuring a convergent Taylor series. Our model necessarily depends on a number of free parameters: these account for the unknown complexities of ultraviolet physics (such as galaxy formation physics and feedback), and ensure physical robustness. Efficient computation of the one-loop bispectrum is nontrivial; as such, we devote a significant portion of this work to discussing its practical computation with the FFTLog algorithm [99]. We compare the theoretical predictions to real- and redshift-space bispectra obtained from the PT Challenge simulations [100], which serve both to validate the approach and to assess the information

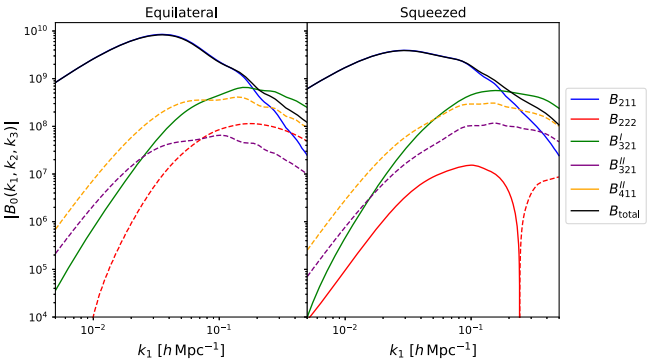

FIG. 1. Contributions to the one-loop galaxy bispectrum monopole in redshift space. The blue and black curves show the tree-level and one-loop bispectra, respectively, with individual one-loop contributions shown in color. Dashed lines indicate negative contributions, and we show results for two types of triangle: equilateral, with $k_1 = k_2 = k_3$, and squeezed, with $k_2 = 0.9k_1$ and $k_3 = 0.2k_1$. For illustration, we assume coevolution biases following [104], with Lagrangian biases $b_1^L = 1$, $b_2^L = 0.3$ and a growth factor $f(z) = 0.7$. We do not include the contributions from stochasticity or counterterms in this plot but note that all bias operators have been renormalized.

content of the one-loop bispectrum model. Though we restrict to the measurement of σ_8 and primordial non-Gaussianity parameters, one can constrain a variety of other phenomena with the bispectrum, and, further still, our methodology can be extended to other correlators including the bispectrum multipoles [65,101] and the recently detected trispectrum [102,103].

The remainder of this paper is structured as follows. The theoretical model is presented in § II, before its implementation is outlined in § III. In § IV we give details of the data and analysis choices used to validate the model, before presenting the results of likelihood analyses using the real- and redshift-space galaxy bispectrum in § V and § VI, respectively. § VII comments on the method's applicability to current datasets, with a summary and discussion given in § VIII. Finally, various technical details are presented in the Appendices: Appendix A discusses the perturbation theory kernels, Appendix B details of the bispectrum integration routines, Appendix C contains a discussion of the redshift-space counterterms, and Appendix D relates the derivation of the stochastic bispectrum components. Appendix E is devoted to prior volume effects. The key plots of this work are Fig. 1, showing the one-loop bispectrum components, and Fig. 4, displaying the utility of the bispectrum for a BOSS-like survey.

II. THEORETICAL MODEL FOR THE ONE-LOOP BISPECTRUM

In this work, we analyze the power spectrum and bispectrum of biased tracers (i.e., galaxies) in redshift space at one-loop order. Whilst the one-loop power spectrum and

tree-level bispectrum have been described in detail before (e.g., [19,80]), a complete model for the one-loop bispectrum has not been presented before (though some aspects can be found in [98]) and will be discussed below, with additional technical details found in the Appendices. Here, we will restrict to Gaussian initial conditions; extension to primordial non-Gaussianity is discussed in § V B.

In the EFT of large scale structure, the bispectrum is comprised of the following terms at one-loop order (e.g., [66,85,105]):

$$B_{1-\rm loop}(\boldsymbol{k}_1,\boldsymbol{k}_2,\boldsymbol{k}_3) = B_{211} + [B_{222} + B^I_{321} + B^{II}_{321} + B_{411}] + B_{\rm ct} + B_{\rm stoch}, \tag{2.1}$$

where the first and second terms give the tree-level and one-loop bispectrum in Eulerian perturbation theory, $B_{\rm ct}$ is the derivative and counterterm contribution, and $B_{\rm stoch}$ encodes stochasticity. This is strictly a function of five variables: three lengths, $\{k_1,k_2,k_3\}$ and two angles, $\{\mu_1,\mu_2\}$, for $\mu_i \equiv \hat{\boldsymbol{k}}_i\cdot\hat{\boldsymbol{n}}$ with line-of-sight $\hat{\boldsymbol{n}}$ (hereafter LOS), noting that $k_1\mu_1 + k_2\mu_2 + k_3\mu_3 = 0$. In real space, this reduces to just three variables: $\{k_1,k_2,k_3\}$.

A. Bias expansion

To compute the bispectrum within Eulerian perturbation theory, our first step is to express real-space galaxy density field, δ_g, in terms of a basis of *bias operators*, i.e., all combinations of the density and velocity fields (δ and θ) consistent with the relevant symmetries up to a given order in perturbation theory [79,106–111]. For the one-loop bispectrum, we require terms up to fourth order (δ_L^4), and here use the basis of Galileon operators proposed in [79]:

$$\begin{aligned}\delta_g = {} & \{b_1\delta\} + \left\{\frac{b_2}{2}\delta^2 + \gamma_2\mathcal{G}_2(\Phi_v)\right\} \\ & + \left\{\frac{b_3}{6}\delta^3 + \gamma_2^\times\delta\mathcal{G}_2(\Phi_v) + \gamma_3\mathcal{G}_3(\Phi_v) + \gamma_{21}\mathcal{G}_2(\varphi_2,\varphi_1)\right\} \\ & + \{\gamma_{21}^\times\delta\mathcal{G}_2(\varphi_2,\varphi_1) + \gamma_{211}\mathcal{G}_3(\varphi_2,\varphi_1,\varphi_1) \\ & + \gamma_{22}\mathcal{G}_2(\varphi_2,\varphi_2) + \gamma_{31}\mathcal{G}_2(\varphi_3,\varphi_1)\} + \mathcal{O}(\delta^5),\end{aligned} \tag{2.2}$$

where curly brackets separate operators of different order and the bias parameters are marked in color. In (2.2), we drop any terms that do not appear in the one-loop bispectrum; these are all composite local evolution operators such as δ^4 and $\delta^2\mathcal{G}_2(\Phi_v)$. Here we have ignored both higher-derivative operators (which we return to below) and bias renormalization, which is discussed in Appendix B. The Galileon operators are defined by

$$\begin{aligned}\mathcal{G}_2(\Phi_v) &\equiv \nabla_i\nabla_j\Phi_v\nabla^i\nabla^j\Phi_v - (\nabla^2\Phi_v)^2, \\ \mathcal{G}_3(\Phi_v) &\equiv 2\nabla_i\nabla_j\Phi_v\nabla^j\nabla_k\Phi_v\nabla^k\nabla^i\Phi_v \\ &\quad - 3\nabla_i\nabla_j\Phi_v\nabla^i\nabla^j\Phi_v\nabla^2\Phi_v + (\nabla^2\Phi_v)^3,\end{aligned} \tag{2.3}$$

where $\Phi_v \equiv \nabla^{-2}\theta$ is the velocity potential, equal to the Newtonian potential $\Phi \equiv \nabla^{-2}\delta$ at leading order. These can be simply generalized to functions of multiple potentials, with (2.2) involving the Lagrangian Perturbation Theory potentials $\varphi_{1,2}$, satisfying

$$\nabla^2\varphi_1 = -\delta, \qquad \nabla^2\varphi_2 = -\mathcal{G}_2(\varphi_1). \tag{2.4}$$

Up to third order, this is equivalent to the bias expansion used in [107] and previous works (e.g., [10,80]), with the relations[1]

$$\gamma_2 \equiv b_{\mathcal{G}_2}, \qquad \gamma_{21} \equiv -\frac{4}{7}(b_{\mathcal{G}_2} + b_{\Gamma_3}). \tag{2.5}$$

Utilizing (2.2), and expanding each operator in terms of the linear density field $\delta^{(1)} \equiv \delta_L$, we can define the nth order contributions to the galaxy density field:

$$\begin{aligned}\delta_g^{(n)}(\boldsymbol{k}) = {} & \int_{\boldsymbol{q}_1\ldots\boldsymbol{q}_n}(2\pi)^3\delta_{\rm D}(\boldsymbol{q}_1\cdots+\boldsymbol{q}_n-\boldsymbol{k}) \\ & \times K_n(\boldsymbol{q}_1,\ldots,\boldsymbol{q}_n)\delta_L(\boldsymbol{q}_1)\cdots\delta_L(\boldsymbol{q}_n),\end{aligned} \tag{2.6}$$

where the real-space kernels K_n are given in Appendix A 1 and depend on the bias parameters given above. Furthermore, this generalizes to the redshift-space density field, $\delta_s(\boldsymbol{k})$, using the well-known mapping (e.g., [112])

$$\delta_g^{(s)}(\boldsymbol{k}) = \delta_g(\boldsymbol{k}) + \int d\boldsymbol{x}\, e^{-i\boldsymbol{k}\cdot\boldsymbol{x}}[e^{-ik_z f u_z(\boldsymbol{x})} - 1](1+\delta_g(\boldsymbol{x})), \tag{2.7}$$

where f is the logarithmic growth rate, $u_z(\boldsymbol{q}) = (i\mu_{\boldsymbol{q}}/q)\theta(\boldsymbol{q})$ is the Fourier-space LOS velocity field, and $\mu_{\boldsymbol{q}} \equiv \hat{\boldsymbol{q}}\cdot\hat{\boldsymbol{n}}$, for LOS vector $\hat{\boldsymbol{n}}$. The associated kernels, analogous to (2.6), are labeled as Z_n and defined for $n \le 4$ in Appendix A 2.

B. Deterministic contributions

Utilizing the redshift-space kernels of Appendix A 2, the tree-level bispectrum, $B_{211} \equiv \langle\delta_g^{(2)}\delta_g^{(1)}\delta_g^{(1)}\rangle$ can be written

$$B_{211}(\boldsymbol{k}_1,\boldsymbol{k}_2,\boldsymbol{k}_3) = 2Z_2(\boldsymbol{k}_1,\boldsymbol{k}_2)Z_1(\boldsymbol{k}_1)Z_1(\boldsymbol{k}_2)P_L(k_1)P_L(k_2) + 2\ \text{cyc.}, \tag{2.8}$$

[1]This is obtained by noting that $\mathcal{G}_2(\Phi_v)$ is just the usual tidal tensor $\mathcal{G}_2 \equiv -\mathcal{G}_2(\delta)$ at first order, and that $\mathcal{G}_2(\varphi_2,\varphi_1)$ is a combination of the $\mathcal{G}_2$ and Γ_3 operators of [107].

where $P_L(k)$ is the linear power spectrum (though see the below discussion on infrared resummation). This depends on the bias parameters, $\{b_1, b_2, \gamma_2\}$, as well as the growth rate, $f(z)$. The one-loop terms can be written as loop integrals over the linear power spectrum and come in four flavors (e.g., [66,105]):

$$\begin{aligned}
B_{222}(\boldsymbol{k}_1,\boldsymbol{k}_2,\boldsymbol{k}_3) &= 8\int_{\boldsymbol{q}} Z_2(\boldsymbol{k}_1+\boldsymbol{q},-\boldsymbol{q})Z_2(\boldsymbol{k}_1+\boldsymbol{q},\boldsymbol{k}_2-\boldsymbol{q})Z_2(\boldsymbol{k}_2-\boldsymbol{q},\boldsymbol{q})P_L(q)P_L(|\boldsymbol{k}_1+\boldsymbol{q}|)P_L(|\boldsymbol{k}_2-\boldsymbol{q}|),\\
B^I_{321}(\boldsymbol{k}_1,\boldsymbol{k}_2,\boldsymbol{k}_3) &= 6Z_1(\boldsymbol{k}_1)P_L(k_1)\int_{\boldsymbol{q}} Z_3(-\boldsymbol{q},\boldsymbol{q}-\boldsymbol{k}_2,-\boldsymbol{k}_1)Z_2(\boldsymbol{q},\boldsymbol{k}_2-\boldsymbol{q})P_L(q)P_L(|\boldsymbol{k}_2-\boldsymbol{q}|)+5\text{ perm.},\\
B^{II}_{321}(\boldsymbol{k}_1,\boldsymbol{k}_2,\boldsymbol{k}_3) &= 6Z_2(\boldsymbol{k}_1,\boldsymbol{k}_2)Z_1(\boldsymbol{k}_2)P_L(k_1)P_L(k_2)\int_{\boldsymbol{q}} Z_3(\boldsymbol{k}_1,\boldsymbol{q},-\boldsymbol{q})P_L(q)+5\text{ perm.},\\
B_{411}(\boldsymbol{k}_1,\boldsymbol{k}_2,\boldsymbol{k}_3) &= 12Z_1(\boldsymbol{k}_1)Z_1(\boldsymbol{k}_2)P_L(k_1)P_L(k_2)\int_{\boldsymbol{q}} Z_4(\boldsymbol{k}_1,\boldsymbol{k}_2,\boldsymbol{q},-\boldsymbol{q})P_L(q)+2\text{ cyc.},
\end{aligned} \tag{2.9}$$

where the B^{II}_{321} spectrum is similar to the $P_{13}(\boldsymbol{k}_1)$ contribution to the one-loop power spectrum. Computation of the loop integrals can be performed via explicit numerical integration or with the FFTLog method [99]; we discuss the latter in § III, with details presented in Appendix B. As well as the tree-level biases, these spectra involve the higher-order parameters $\{b_3, \gamma_2^\times, \gamma_3, \gamma_{21}, \gamma_{21}^\times, \gamma_{211}, \gamma_{22}, \gamma_{31}\}$, of which only γ_{21} appears in the one-loop power spectrum.

C. Counterterms

To ensure a self-consistent theoretical model, we require a set of counterterms, which account for nonidealities in fluid equations (via the viscous stress tensor), and absorb the unknown ultraviolet (UV, $q \gg k$) behavior of the loop integrals in (2.9) (e.g., [66,67,85]). For the one-loop bispectrum in real space, these operators are degenerate with derivative operators in the bias expansion, such as $\nabla^2\delta$. Furthermore, the redshift-space bispectrum contains additional counterterms that appear after the renormalization of contract operators in the perturbative mapping of (2.7); these are discussed in detail in Appendix C.

The overall bispectrum counterterm contribution can be written as

$$\begin{aligned}
B_{\rm ctr}(\mathbf{k}_1,\mathbf{k}_2,\mathbf{k}_3) = {}& 2Z_1(\mathbf{k}_1)Z_1(\mathbf{k}_2)(F_2^{\rm ctr}+Z_2^{\rm ctr})\\
&\times(\mathbf{k}_1,\mathbf{k}_2)P_L(k_1)P_L(k_2)+\text{cyclic perms.},
\end{aligned} \tag{2.10}$$

where $F_2^{\rm ctr}(\mathbf{k}_1,\mathbf{k}_2)$ is the real-space counterterm kernel [79]:

$$\begin{aligned}
F_2^{\rm ctr}(\boldsymbol{k}_1,\boldsymbol{k}_2) = {}& -\{[\beta_{B,a}(k_1^2+k_2^2)+\beta_{B,b}k_3^2]F_2(\boldsymbol{k}_1,\boldsymbol{k}_2)\\
&+[\beta_{B,c}(k_1^2+k_2^2)+\beta_{B,d}k_3^2]\kappa(\boldsymbol{k}_1,\boldsymbol{k}_2)\\
&+\beta_{B,e}\boldsymbol{k}_1\cdot\boldsymbol{k}_2\}\frac{1}{k_{\rm NL}^2},
\end{aligned} \tag{2.11}$$

where $\kappa(\boldsymbol{k}_1,\boldsymbol{k}_2) = (\hat{\boldsymbol{k}}_1\cdot\hat{\boldsymbol{k}}_2)-1$ (cf. Appendix (A2), and we choose the nonlinear scale $k_{\rm NL} = 0.45\,h\,{\rm Mpc}^{-1}$ [44,113,114].[2] Equation (2.10) additionally involves the μ-dependent redshift-space kernel $Z_2^{\rm ctr}$ defined by

$$\begin{aligned}
Z_2^{\rm ctr}(\mathbf{k}_1,\mathbf{k}_2) = \frac{1}{k_{\rm NL}^2}\Bigg({}& C_1k_{3z}^2F_2(\mathbf{k}_1,\mathbf{k}_2)+C_2k_{3z}^2\left(\mu_3^2-\frac{1}{3}\right)F_2(\mathbf{k}_1,\mathbf{k}_2)+C_3k_{3z}^2+C_4k_{3z}^2\left(\frac{(\mathbf{k}_1\cdot\mathbf{k}_2)\mu_1\mu_2}{k_1k_2}-\frac{\mu_1^2+\mu_2^2}{3}+\frac{1}{9}\right)\\
&+C_5fk_{3z}^2\mu_3^2G_2(\mathbf{k}_1,\mathbf{k}_2)+C_6fk_{3z}^3\left[\frac{\mu_1}{k_1}\left(\mu_2-\frac{1}{3}\right)+\frac{\mu_2}{k_2}\left(\mu_1-\frac{1}{3}\right)\right]+C_7fk_{3z}^3\left[\frac{\mu_1}{k_1}+\frac{\mu_2}{k_2}\right]\\
&+C_8f^2k_{3z}^4\frac{\mu_1}{k_1}\frac{\mu_2}{k_2}+C_9k_{3z}^2\left(\frac{(\mathbf{k}_1\cdot\mathbf{k}_2)^2}{k_1^2k_2^2}-\frac{1}{3}\right)\Bigg),
\end{aligned} \tag{2.12}$$

as derived in Appendix C, with $k_{3z} \equiv k_3\mu_3$. In principle, two combinations of C_1, C_2, and C_5 are constrained by the power spectrum, so only one parameter out of three is independent here. In practice, however, we did not find any difference between imposing the power spectrum constraints on C_1, C_2, C_5 or treating them as free parameters. This is why we proceed with keeping them free in what follows. In total, the one-loop bispectrum counterterm depends on 14 free parameters, $\{\beta_{B,i}\}$, and

[2]The nonlinear scale at redshift z is conventionally defined as $\frac{1}{2\pi^2}P_L(z;k_{\rm NL})k_{\rm NL}^3 = 1$.

$\{C_i\}$ in addition to the one-loop power spectrum counterterms.[3]

Notably, many of the counterterms appearing in (2.12) are degenerate at the bispectrum monopole level; nevertheless, we prefer to keep all of them in the model, and marginalize over them within physically motivated priors. This is done for two main reasons. First, terms with different powers of μ can, in principle, be distinguished even at the bispectrum monopole level thanks to the Alcock-Paczynski projection effect [115], which is described below. Second, the degeneracy between these terms can be broken with higher order angular multipole moments of the bispectrum [37,41], which we will analyze in the future.

D. Stochasticity

Contributions to the bispectrum are also sourced by the nondeterministic part of the density field ϵ [107–111], i.e., that uncorrelated with δ_L. At tree-level, this gives two terms, $\propto 1/\bar{n}^2$, $P(k)/\bar{n}$ (arising from Poissonian shot-noise with sample density $\bar{n}$), whilst at one-loop order, we must keep contributions suppressed by $(kR_*)^2$, where R_* is some characteristic halo size of the order of the halos Lagrangian radius. For the mock galaxy sample we are interested in, this scale is parametrically similar to $k_{\rm NL}^{-1}$. Hence, we will use $k_{\rm NL}$ in order to normalize all nuisance parameters in what follows. We stress that since we vary all the nuisance coefficients as free parameters, the choice $R_* \sim k_{\rm NL}^{-1}$ is arbitrary and will not affect our results.

From [79], we have the following form at next-to-leading order in real space:

$$B_{\rm stoch}(\boldsymbol{k}_1,\boldsymbol{k}_2,\boldsymbol{k}_3)|_{\rm real-space} = \frac{A_{\rm shot,0}}{\bar{n}^2} + \frac{A_{\rm shot,1}}{\bar{n}^2}(k_1^2+k_2^2+k_3^2) + \left[\left(B_{\rm shot} + S_1\frac{k_1^2}{k_{\rm NL}^2} + S_0\frac{k_2^2+k_3^2}{k_{\rm NL}^2}\right)\frac{P_L(k_1)}{\bar{n}} + 2\,\text{cyc.}\right], \tag{2.13}$$

depending on another five free parameters $\{A_{\rm shot,0}, B_{\rm shot}\}$ and $\{A_{\rm shot,1}, S_0, S_1\}$, which cannot be constrained with the one-loop power spectrum. In the Poisson limit, $A_{\rm shot,0} = B_{\rm shot} = 1$, with all higher-order terms (arising, for example, from halo exclusion) vanish.

In redshift space, significantly more dependencies arise. A systematic derivation of these is presented in Appendix D and yields the following expression:

$$B_{\rm stoch} = B_{\rm stoch}^{(P\bar{n}^{-1})} + B_{\rm stoch}^{(\bar{n}^{-2})} + B_{\rm stoch}^{(k^2P\bar{n}^{-1})} + B_{\rm stoch}^{(k^2\bar{n}^{-2})}, \tag{2.14}$$

where

$$\begin{aligned}
B_{\rm stoch}^{(P\bar{n}^{-1})}(\mathbf{k}_1,\mathbf{k}_2,\mathbf{k}_3) &= [b_1 B_{\rm shot} + f\mu^2(1+P_{\rm shot})]\frac{Z_1(\mathbf{k}_1)P_L(k_1)}{\bar{n}} + \text{cyc.},\\
B_{\rm stoch}^{(\bar{n}^{-2})}(\mathbf{k}_1,\mathbf{k}_2,\mathbf{k}_3) &= \frac{A_{\rm shot,0}}{\bar{n}^2},\\
B_{\rm stoch}^{(k^2P\bar{n}^{-1})}(\mathbf{k}_1,\mathbf{k}_2,\mathbf{k}_3) &= \left[\sum_{n=1,2,3,4} S_n k_1^2\mu_1^{2(n-1)} + S_5 Z_1(\mathbf{k}_1)(\mu_2^2k_2^2+\mu_3^2k_3^2) + S_6 Z_1(\mathbf{k}_1)\mu_1^2(\mu_2^2k_2^2+\mu_3^2k_3^2)\right.\\
&\quad \left. + S_7 Z_1(\mathbf{k}_1)\frac{k_{1z}}{k_1^2}(k_{2z}^3+k_{3z}^3) + S_0 Z_1(\mathbf{k}_1)(k_2^2+k_3^2)\right]\frac{P_L(k_1)}{k_{\rm NL}^2\bar{n}} + \text{cyc.},\\
B_{\rm stoch}^{(k^2\bar{n}^{-2})}(\mathbf{k}_1,\mathbf{k}_2,\mathbf{k}_3) &= [A_{\rm shot,1}(k_1^2+k_2^2+k_3^2) + A_{\rm shot,2}(k_{3z}^2+k_{1z}^2+k_{2z}^2)]\frac{1}{k_{\rm NL}^2\bar{n}^2}.
\end{aligned} \tag{2.15}$$

This expression shares the parameter $P_{\rm shot}$ with the power spectrum, but it includes an additional 12 nuisance coefficients: $\{\{S_n\}, \{A_{\rm shot,n}\}, B_{\rm shot}\}$. $P_{\rm shot}$ is defined as a constant rescaling of the stochastic power spectrum [80],

$$\langle\epsilon(\mathbf{k})\epsilon(\mathbf{k}')\rangle = (2\pi)^3\delta_D^{(3)}(\mathbf{k}+\mathbf{k}')\frac{1+P_{\rm shot}}{\bar{n}}. \tag{2.16}$$

Note that in the absence of projection effects the counterterms $A_{\rm shot,1}$ and $A_{\rm shot,2}$ are fully degenerate. Therefore, for the purposes of this study we will set $A_{\rm shot,2} = 0$.

In addition, we note that with the definition (2.16) the parameter $P_{\rm shot}$ can be negative in the presence of the halo exclusion effects [116–119].

E. Infrared resummation

An additional complication arises from the effects of long-wavelength displacements, which can be consistently treated using "infrared resummation." A rigorous derivation

[3]Some of the bispectrum counterterms are time integrals of the power spectrum counterterms, but since we do not know the time dependence, we prefer to keep all the counterterms free.

of this was presented in [86,87] in the context of time-sliced perturbation theory [120], and, at tree-level order, can be implemented by replacing the linear power spectrum P_L with its IR-resummed equivalent, i.e.,[4]

$$P_L(k) \to P_{nw}(k) + e^{-\Sigma^2 k^2(1+f\mu^2(2+f))-\delta\Sigma^2 k^2 f^2\mu^2(\mu^2-1)} P_w(k) \equiv P_{nw}(k) + e^{-\Sigma^2_{\rm tot}(\mu)k^2} P_w(k), \tag{2.17}$$

where P_w and P_{nw} are the wiggly and smooth parts of the power spectrum, respectively. This has the effect of damping the oscillatory component by a k- and μ-dependent factor. The damping scales are given in terms of the broadband power spectrum as

$$\Sigma^2 = \frac{1}{6\pi^2}\int_0^{k_S} dq\, P_{nw}(q)[1 - j_0(qr_{\rm BAO}) + 2j_2(qr_{\rm BAO})],$$
$$\delta\Sigma^2 = \frac{1}{2\pi^2}\int_0^{k_S} dq\, P_{nw}(q) j_2(qr_{\rm BAO}), \tag{2.18}$$

where $r_{\rm BAO}$ is the sound-horizon scale and $k_S \sim 0.1\,h\,{\rm Mpc}^{-1}$. At one-loop order, the IR-resummed bispectrum can be written schematically as

$$B_{1-{\rm loop}} = B_{211}[P_{nw} + (1+k^2\Sigma^2_{\rm tot})e^{-\Sigma^2_{\rm tot}k^2}P_w] + (B^I_{321} + B^{II}_{321} + B_{411})[P_{nw} + e^{-\Sigma^2_{\rm tot}k^2}P_w], \tag{2.19}$$

where $B[P]$ indicates that the bispectrum should be evaluated using the power spectrum P and we have dropped the counterterms and stochasticity [86]. In this case, the loop corrections become more complex, since the damping factor, $\Sigma^2_{\rm tot}$, is a function of the redshift-space angles μ. To allow for efficient computation via the FFTLog procedure (Appendix B), we here adopt the isotropic approximation for the one-loop terms, dropping any μ dependence in $\Sigma^2_{\rm tot}$ inside the integral. This is expected to be a good approximation in practice, and is exact for the real-space case. Note that we keep the full redshift-dependent damping function in the tree-level expressions, i.e., the isotropic templates are used only for the computations of the one-loop corrections.

We will see shortly that the use of the isotropic approximation for the damping factor inside the loop corrections does not lead to any bias in the PT Challenge data analysis. The volume of this simulation is larger than the volumes of current and future surveys like BOSS, DESI, and Euclid. This strongly suggests that the isotropic damping approximation will be adequate for the precision of these surveys.

[4]Note that the general expressions for the IR resummed functions in terms of differential operators presented in [86,87] can be applied to the whole power spectrum, i.e., in principle the procedure of these works does not require a wiggly smooth decomposition. We prefer to use this decomposition because it results in a significant time gain.

F. Coordinate rescalings

To compare to observations, we must distill the full bispectrum $B(\boldsymbol{k}_1, \boldsymbol{k}_2, \boldsymbol{k}_3)$ to a lower-dimensional form. In this work, we consider the angle-averaged bispectrum monopole (as in [15,80,96]), defined via

$$B_0(k_1,k_2,k_3) = \int_{-1}^1 \frac{d\mu}{2}\int_0^{2\pi}\frac{d\phi}{2\pi} B(k_1,k_2,k_3,\mu_1[\mu],\mu_2[\mu,\phi]), \tag{2.20}$$

in terms of the angles μ and ϕ, with $\mu_1 = \mu$, $\mu_2 = \mu\cos\alpha - \sqrt{1-\mu^2}\sin\alpha\cos\phi$, for $\cos\alpha \equiv \hat{\boldsymbol{k}}_1\cdot\hat{\boldsymbol{k}}_2$. In practice, we must consider also the impact of the fiducial cosmology used to convert angles and redshifts into Cartesian coordinates: this modifies (2.20) to

$$B_0(k_1,k_2,k_3) = \frac{1}{\alpha_\parallel^2\alpha_\perp^4}\int_{-1}^1\frac{d\mu}{2}\int_0^{2\pi}\frac{d\phi}{2\pi} \times B(q_1[k_1,\mu_1], q_2[k_2,\mu_2], q_3[k_3,\mu_3], \nu_1[\mu], \nu_2[\mu_2(\mu,\phi)]), \tag{2.21}$$

with $q = k\sqrt{\mu^2/\alpha_\parallel^2 + (1-\mu^2)/\alpha_\perp^2}$ and $\nu = \mu/[\alpha_\parallel\sqrt{\mu^2/\alpha_\parallel^2 + (1-\mu^2)/\alpha_\perp^2}]$ for conventional rescaling parameters $\alpha_\parallel$, $\alpha_\perp$ depending on cosmological parameters [80]. The angular integrals can be performed numerically via Gauss-Legendre quadrature in practice. We further incorporate integration over finite k bins as well as discreteness effects; both effects are discussed below.

III. PRACTICAL IMPLEMENTATION

A. Loop integrals

We now discuss how to compute the one-loop bispectrum. The most difficult part of this is evaluating the loop integrals appearing in (2.9): in this work, these are computed via the FFTLog procedure [99], the subtleties of which are described in Appendix B. In essence, the real-space computation proceeds by first writing the integration kernels (products of Z_n) as polynomials in k_i^2, q^2, and $|\boldsymbol{k}_i \pm \boldsymbol{q}|^2$ (or their reciprocals). By expanding the linear (or IR resummed) power spectrum as a sum over complex polynomials, i.e., $P_L(k) \sim \sum c_m k^{\nu+i\eta_m}$ for frequency η_m and FFTLog "bias" ν, the various terms in (2.9) take the form (using B_{222} as an example)

$$\sum_{m_1m_2m_3} c_{m_1}c_{m_2}c_{m_3}\int_{\boldsymbol{q}}\frac{1}{q^{2\nu_1}|\boldsymbol{k}_1-\boldsymbol{q}|^{2\nu_2}|\boldsymbol{k}_2+\boldsymbol{q}|^{2\nu_3}} \tag{3.1}$$

for some complex ν_i. The integral can be evaluated using techniques borrowed from quantum field theory and reduces the calculation to a tensor multiplication, noting that all cosmological information is encoded within c_m. In redshift space, the appearance of angles, $\hat{\boldsymbol{q}}\cdot\hat{\boldsymbol{n}}$ inside the integral make this more challenging; however, it can be evaluated using similar tricks to the one-loop power spectrum (cf. [113]), as discussed in Appendix B.

Following the above tricks, the bispectrum takes the following schematic form, again taking B_{222} as an example:

$$B_{222}(k_1,k_2,k_3,\mu_1,\mu_2)\sim\sum_i\theta_i\sum_{0\le j+k\le 12}\mu^j\chi^k B_{222}^{(i,j,k)}(k_1,x,y), \tag{3.2}$$

where the i index runs over all combinations of bias and $f(z)$, denoted θ_i.[5] Additionally, we have expanded in terms of the redshift-space angles $\{\mu,\chi\equiv\sqrt{1-\mu^2}\cos\phi\}$ (of which there are 47 nontrivial combinations); these are related to the μ_i angles via

$$\mu_1\equiv\mu,\quad \mu_2\equiv\mu\cos\alpha-\chi\sin\alpha,\quad k_3\mu_3=-k_1\mu_1-k_2\mu_2. \tag{3.3}$$

We adopt this basis rather than the more familiar choice of $\{\mu_1,\mu_2\}$, since it avoids pathologies for flattened triangles (whence $k_1\approx k_2+k_3$, and $\mu_1\approx-\mu_2$). The underlying shapes, $B^{(i,j,k)}$, appearing in (3.2) are independent of both redshift-space angles and bias parameters, and depend only on the form of the linear power spectrum, k_1, $x=k_3^2/k_1^2$ and $y=k_2^2/k_1^2$, assuming $k_1\ge k_2\ge k_3$.

Two options arise for using the bispectrum templates $B^{(i,j,k)}$ in Monte Carlo Markov chain (MCMC) analyses: (1) they may be computed once for a fixed linear power spectrum, (2) they may be computed as a tensor multiplication [cf. (3.1)] at each step in the MCMC chain, feeding in the relevant linear power spectrum (and thus c_m coefficients) each iteration. Whilst (2) is the approach usually adopted for the one-loop power spectrum, we will here adopt (1) for the one-loop bispectrum. This has the effect of fixing cosmology in the bispectrum loops (except for σ_8, which acts as a global rescaling, modulo a small effect concerning the IR resummation amplitude, which we ignore in this work), and is chosen on computational grounds, since the size of the necessary FFTLog matrices becomes very large.[6] Explicitly, we compute the bispectrum templates, $B^{(i,j,k)}$, for a grid of values of $\{x,y,k_1\}$ (treating flattened triangles with $\sqrt{x}+\sqrt{y}=1$ separately to avoid divergences), then use these to construct a three-dimensional linear interpolator for each shape. The resulting bispectra have been compared to results from explicit (and computationally intensive) numerical integration for a range of values of bias and triangle shapes and found to be in excellent agreement. Full details of the above steps are given in Appendix B 3. We additionally publicly release all our analysis code: this can be found at GitHub.com/OliverPhilcox/OneLoopBispectrum.

[5]Examples of these include b_1^3, $\gamma_2 b_1 f^2$, f^6 *et cetera*.

[6]To see this, note that the matrix in (3.1) has size $N_{\rm freq}^3$, for $N_{\rm freq}$ FFTLog frequencies. Taking $N_{\rm freq}=64$, with 47 angular combinations, $\mathcal{O}(50)$ bias parameter combinations, and computing the matrix for 10 choices of each of x and y (noting that k scales out), we find $\sim5\times10^{10}$ elements, or ~50 GB in (complex) single precision.

B. Bin integration

To robustly compare theory and data, we must integrate the model across some set of bins. Following [80], this is achieved via the integral:

$$\hat{B}_{0,\rm int}=\frac{V^2}{(2\pi)^6N_{123}}\prod_{i=1}^3\left(\int_{k_i-\Delta k/2}^{k_i+\Delta k/2}dq_iq_i\right)B_0(q_1,q_2,q_3), \tag{3.4}$$

where B_0 is the bispectrum monopole of (2.21) and $N_{123}=8\pi k_1k_2k_3(\Delta k)^3V^2/(2\pi)^6$ for bin center (k_1,k_2,k_3) and width Δk. As in [80], this is strictly exact only in the narrow-bin limit, and can be corrected by "discreteness weights" as in the former work. In practice, we compute the set of bispectrum templates $B^{(i,j,k)}(k_1,x,y)$ for a range of values of k_1,x,y (see Appendix B 3) then perform the bin averaging by linearly interpolating these values, dropping any triangles that do not satisfy the triangle conditions $|q_1-q_2|\le q_3\le q_1+q_2$. The integration is performed using Gauss-Legendre quadrature, as for the angular integrals. Finally, we note that we can perform bin integration either within the MCMC chains or as a preprocessing step (allowing us to use bin-averaged templates in the later analysis). We use the latter option for the purposes of this paper.

C. Free parameters

Our full model for the one-loop galaxy power spectrum and bispectrum depends on the following 44 free parameters (i.e., Wilson coefficients):

$$\begin{aligned}&\{b_1,b_2,b_{\mathcal{G}_2},b_3,\gamma_2^\times,\gamma_3,b_{\Gamma_3},\gamma_{21}^\times,\gamma_{211},\gamma_{22},\gamma_{31}\}\\&\times\{c_0,c_2,c_4,\tilde{c},\beta_{B,a},\beta_{B,b},\beta_{B,c},\beta_{B,d},\beta_{B,e},C_i[i=1\ldots9]\}\\&\times\{P_{\rm shot},a_0,a_2,B_{\rm shot},A_{\rm shot,0},A_{\rm shot,1},S_i[i=0\ldots7]\},\end{aligned} \tag{3.5}$$

where parameters appearing only in the power spectrum (following the definitions of [80]), only in the bispectrum, and in both spectra, are shown in blue, black, and purple, respectively. The three lines give bias parameters, UV counterterms, and stochasticity parameters, respectively.

Note that here we switch to the power spectrum biases $b_{\mathcal{G}_2}$ and b_{Γ_3} instead of γ_2 and γ_{21} to ease the comparison with previous works [80,121]; these are related via (2.5). Whilst performing an MCMC analysis in this high-dimensional space may seem a formidable task, we note that all parameters except $\{b_1, b_2, b_{\mathcal{G}_2}\}$ enter the theory model linearly, and can thus be analytically marginalized, following [122]. This is exact, and will be applied to all analyses presented in this work, significantly reducing computational cost. Since the parameter b_{Γ_3} is of physical interest in power spectrum analyses, we opt to marginalize over this explicitly, alongside the quadratic biases.

For the purposes of the analytic marginalization, we assume the following priors on the bispectrum nuisance parameters: all means are zeros, and the expectation values given by 10 for all bias parameters, 10 for all real-space counterterms, and one-loop stochastic contributions, 20 for redshift-space counterterms (in order to account for enhancements caused by short-scale nonlinear redshift-space distortions, known as fingers of God [123]), and 20 for redshift-space one-loop stochastic contributions. For the tree-level stochastic counterterms, following [80] we assume standard deviations of 5 for the dimensionless $B_{\rm stoch}$, $P_{\rm shot}$, and $A_{\rm shot}$ parameters. The power spectrum nuisance priors match [80,121]. Note that our nuisance parameters are normalized in such a way that their physical values are expected to be $\mathcal{O}(1)$ numbers from the naturalness arguments. In this sense our physically motivated choice of nuisance parameter is conservative, as we allow them to be as large as $\mathcal{O}(10)$.

D. Numerical results

Before proceeding to use the one-loop bispectra to perform parameter inference, we first consider the form of the spectra themselves. Plotting the bispectrum is a challenge itself: the monopole exists in the three-dimensional simplex of $\{k_1, k_2, k_3\}$, and we have contributions from a wide variety of nuisance parameter combinations. For the purpose of visualization, we will fix the bias parameters to simple local-in-Lagrangian space predictions, based on [104]: assuming the bias to be described only by linear and quadratic terms b_1^L, b_2^L in Lagrangian space, this gives

$$\begin{aligned}&\Big\{b_1 = b_1^L + 1, b_2 = b_2^L, b_3 = -3b_2, \gamma_2 = -\frac{2}{7}b_1^L, \gamma_3 = -\frac{1}{9}b_1^L - \gamma_2,\\ &\gamma_{21} = \frac{2}{21}b_1^L + \frac{6}{7}\gamma_2, \gamma_2^\times = -\frac{2}{7}b_2, \gamma_{22} = -\frac{6}{539}b_1^L - \frac{9}{49}\gamma_2\\ &\gamma_{21}^\times = \frac{2}{21}b_2 + \frac{2}{7}\gamma_2^\times, \gamma_{31} = -\frac{4}{11}b_1^L - 6\gamma_2, \gamma_{211} = \frac{5}{77}b_1^L + \frac{15}{14}\gamma_2 + \gamma_{21} - \frac{9}{7}\gamma_3\Big\}.\end{aligned} \tag{3.6}$$

In Fig. 1 we plot the deterministic (Eulerian PT) bispectrum contributions assuming the above bias relations with $b_1^L = 1$, $b_2^L = 0.3$ and $f(z) = 0.7$, as well as distortion parameters $\alpha_\parallel = \alpha_\perp = 1$ and the best-fit PT Challenge input power spectrum (cf. §IV). For both equilateral and squeezed triangles we observe a similar form: the one-loop corrections are suppressed on large scales (by $k/k_{\rm NL}$) but become large as k increases, with the B_{321}^I piece exceeding tree-level theory by $k \sim 0.1\,h\,{\rm Mpc}^{-1}$. We find significant cancellation between the various one-loop components (which all depend on the same biases), which is expected from the IR cancellation of loop integrals. Note that the high-k behavior is further modified by the counterterms [scaling as $k^2 P_L^2(k)$] and stochasticity [scaling as k^0 and $P_L(k)$ at leading order]. The individual shapes of the bispectrum components are generally nontrivial, with oscillatory signatures seen in B_{411} and, to a lesser extent, $B_{321}^{I,II}$. The smooth nature of B_{222} (expected since the three power spectra are all inside the $\boldsymbol{q}$ integral) implies that a smaller number of FFTLog frequencies can likely be used in its computation, which may expedite the template computation, and suggests that this has only weak cosmology dependence. From the deterministic contributions alone, it is clear that the one-loop bispectrum is a significant fraction of $B_{\rm tree}$ for all $k \gtrsim 0.1\,h\,{\rm Mpc}^{-1}$, and thus its inclusion is necessary if we wish to model the bispectrum beyond the softest modes.

IV. DATA AND ANALYSIS DETAILS

The dataset used in this paper is the PT Challenge suite [100], comprising high-resolution N-body simulations at $z = 0.61$ with a total volume of $566\,h^{-3}\,{\rm Gpc}^3$. Galaxies are allocated via a BOSS-like halo occupation prescription, and various summary statistics computed using a fiducial cosmology with $\Omega_m = 0.3$. In all our analyses, we use the redshift-space power spectrum multipoles, $P_\ell(k)$, and the real-space power spectrum proxy Q_0,

$$Q_0(k) \equiv P_0(k) - \frac{1}{2}P_2(k) + \frac{3}{8}P_4(k), \tag{4.1}$$

both of which were studied in detail in [121]. In this work, we additionally add the bispectra in both real and redshift space, with the comparison allowing us to assess the

relative importance of redshift-space distortions in the one-loop bispectrum.

The relevant bispectra are computed as described in [80], which studied the tree-level bispectrum likelihood. We bin the bispectrum data in wave number bins of width $\Delta k = 0.01\,h\,\mathrm{Mpc}^{-1}$, and use only triangles whose bin centers satisfy momentum conservation.[7] For $k_{\rm max} = 0.15, 0.2, 0.3$, we find a total of 372, 825, and 2600 independent triangle configurations, respectively, and note that, unlike [80], we do not include the very first bin in the analysis, i.e., we fix $k_{\rm min} = 0.01\,h\,\mathrm{Mpc}^{-1}$ for the bispectrum. This matches the analyses of the actual surveys like BOSS, where the very first bin is often affected by systematics including stellar contamination [2,15].

Note that we have chosen the bispectrum binning to be the optimal with respect to two factors. On the one hand, the binning cannot be too coarse since in this case we will smooth out shape features in the bispectrum and loose cosmological information. On the other hand, the binning cannot be very narrow, because in this case it may be more difficult to take into account the discreteness effects, and also the size of the bispectrum data vector would significantly increase, thereby slowing down the analysis. Based on these reasons we chose $\Delta k = 0.01\,h/\mathrm{Mpc}$, which yields a reasonable size of the data vector and which is still sufficiently narrow to resolve spectral features such as the baryon acoustic oscillation (BAO).

Our theory model for the power spectrum matches that of [80,121], and we make use of the publicly available code CLASS-PT [113] to compute the power spectrum models.[8] Similarly, our theoretical model for the bispectrum is discussed in detail in Sec. II, and implemented using the FFTLog prescription using *Mathematica*—we refer the reader to Appendix B for technical details.

An important part of the likelihoods are the covariance matrices, encoding both errors and correlations. As in previous works, we here adopt the Gaussian tree-level approximation for the analytic covariance matrices of power spectra and bispectra, neglecting any cross-correlation between the two statistics. For sufficiently large scales these assumptions are well justified [24,63,65,80]; at smaller scales, and in the presence of nonuniform survey geometry, a mock-based approach will probably be needed, such as in [15], most likely in combination with some compression scheme (e.g., [122]). In this work we use the bispectrum data in the range $0.1 \lesssim k_{\rm max}/(h\,\mathrm{Mpc}^{-1}) \lesssim 0.2$, so that the deviations from the Gaussian tree-level covariance approximation are small but not completely negligible, see, e.g., [35,45,124–126]. These references found that neglecting non-Gaussian contributions to the bispectrum covariance matrix and the mixed covariance between the power spectrum and the bispectrum can overestimate the errorbar on σ_8 by ∼20% at $k_{\rm max} = 0.1\,h\,\mathrm{Mpc}^{-1}$. This caveat should be borne in mind when interpreting our results.

The mock galaxy clustering data from the PT Challenge simulations are analyzed within the Bayesian framework. Here, we perform a global MCMC analysis using the publicly available sampler MONTEPYTHON [127,128] varying the clustering amplitude σ_8, $f_{\rm NL}^{\rm equil}$ (the amplitude of equilateral primordial non-Gaussianity [96]) and the EFT nuisance parameters. Since the true value of σ_8 in the simulations remains blinded, we will show results only for the fractional error on σ_8. As noted above, we will marginalize over all physical nuisance parameters given in § III C. This is in contrast with some bispectrum studies that aim to fix certain nuisance parameters, such as asserting coevolution relations for Lagrangian biases [81]. Indeed, for some particular purposes, i.e., fits of σ_8, it may be sufficient to keep fewer parameters in the fit. However, such approximations are unwarranted—their validity can break down for other types of analyses. Therefore, we prefer to explicitly vary all physical nuisance parameters in the fit. By virtue of analytic marginalization [122], this is done at no computational cost.

V. RESULTS: REAL SPACE

We now present results from the above analyses, focusing first on the combination of the redshift-space power spectrum and real-space bispectrum. Though not quite matching observational setups (where the power spectrum and bispectrum are both observed in redshift space), this analysis will allow us to understand the impact of redshift-space distortions.

To obtain the real space model, we set $f = 0$ in all calculations and retain only EFT operators that do not depend on the LOS angles, giving a one-loop model fully equivalent to that used in [79,81]. Our data vector contains the power spectrum multipoles, the real-space analog and the bispectrum monopole, i.e., $[P_\ell(k), Q_0(k), B(k_1, k_2, k_3)]$ and we restrict to the $z = 0.61$ snapshot of the PT Challenge simulations. In most analyses we use $P_\ell(k)$ up to $k_{\rm max} = 0.16\,h\,\mathrm{Mpc}^{-1}$, and Q_0 in the range $0.16\,h\,\mathrm{Mpc}^{-1} \leq k < 0.40\,h\,\mathrm{Mpc}^{-1}$, as validated in [80,100,121]. We explore the impact of varying the bispectrum $k_{\rm max}$ below.

A. Clustering amplitude and bias parameters

We first focus on measuring the mass clustering amplitude σ_8 and leading galaxy bias parameters $\{b_1, b_2, b_{\mathcal{G}_2}, b_{\Gamma_3}\}$. These appear both in the one-loop power spectrum and bispectrum models, and hence can be tightly constrained by the data. Unlike σ_8, the true values of bias parameters in the simulations are unknown. As such, we take their best-fit values at a certain $k_{\rm max}$ (where the one-loop model can be

[7] As shown in [80], the remaining triangles do not carry significant cosmological information.

[8] GitHub.com/michalychforever/CLASS-PT.

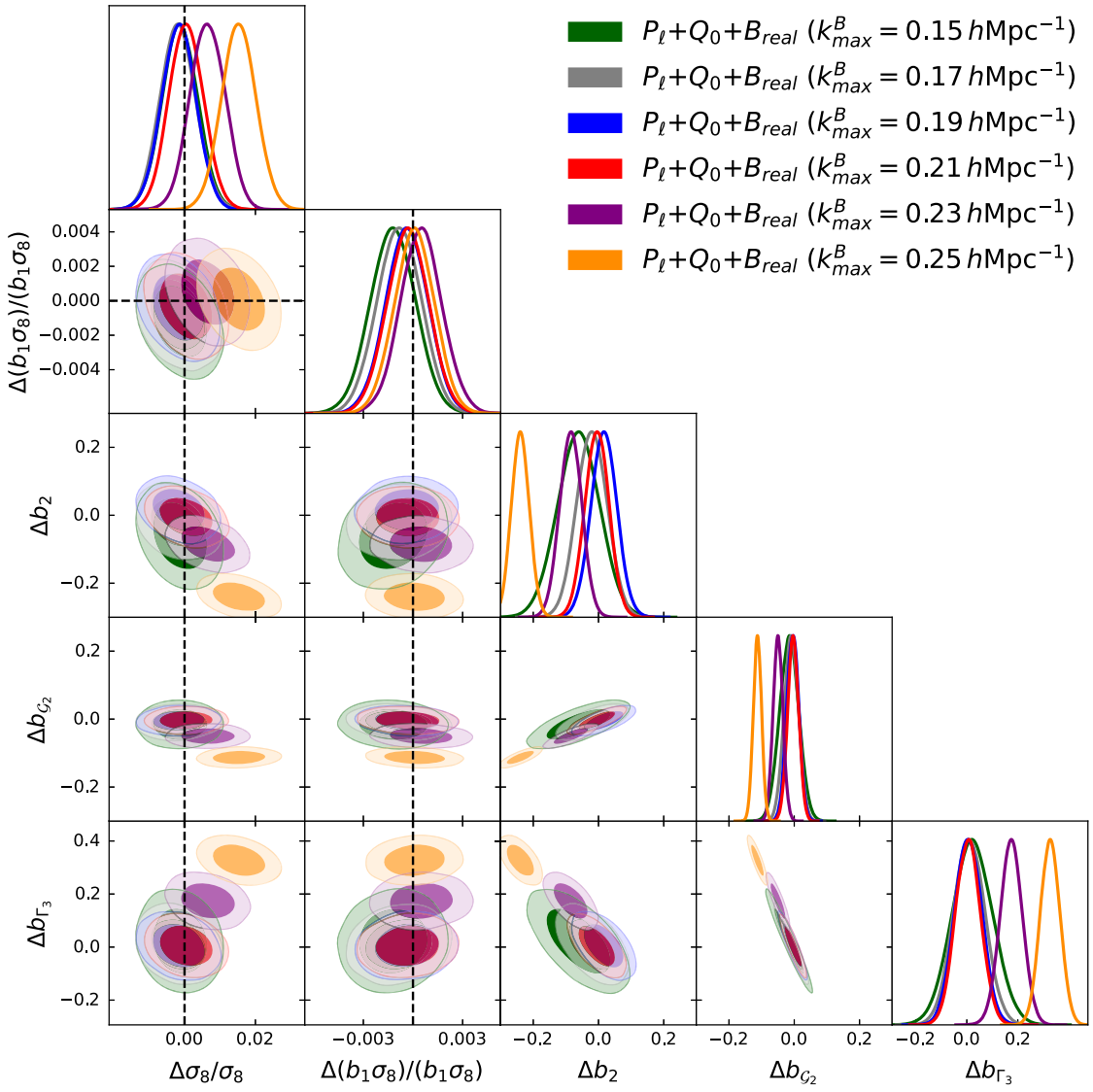

FIG. 2. Posterior distributions for the clustering amplitude, σ_8, and certain nuisance parameters extracted from MCMC analyses of the power spectrum multipoles and the one-loop real-space bispectrum. The power spectrum likelihood is the same for all cases, whilst we vary $k^B_{\rm max}$ for the bispectrum, as indicated in the caption. Corresponding marginalized parameter contours for $k_{\rm max} = 0.21\,h\,{\rm Mpc}^{-1}$ are given in Table I.

trusted) as a proxy for their true values. This $k_{\rm max}$ is measured as in [100] (see also [114]) by determining at what scale cut posteriors for at least one parameter become biased with respect to analyses with lower $k_{\rm max}$. We take best-fit values of bias parameters at the last stable $k_{\rm max}$ as ground truth, $p_{\rm true}$. Following this, our parameter measurements are quoted as $\Delta p = p - p_{\rm true}$ to avoid unblinding the results.

We fit the real-space bispectrum data for the following choices of scale cuts:

$$k^B_{\rm max}/(h\,{\rm Mpc}^{-1}) = 0.15, 0.17, 0.19, 0.21, 0.23, 0.25.$$

The resulting posterior contours are shown in Fig. 2, with one-dimensional marginalized limits on the amplitude and some nuisance parameters shown in Table I. From the figure, we find that the posterior on σ_8 remains unbiased up to $k^B_{\rm max} = 0.21\,h\,{\rm Mpc}^{-1}$, with a shift of 1–2% observed for $k^B_{\rm max} = 0.23\,h\,{\rm Mpc}^{-1}$ and $k^B_{\rm max} = 0.25\,h\,{\rm Mpc}^{-1}$, which becomes significant relative to the PT Challenge error bars.

However, at $k^B_{\rm max} \geq 0.23\,h\,{\rm Mpc}^{-1}$, we observe that the nuisance parameters become biased with respect to measurements at low scale cuts, for example, we find a visible tension between the b_2 posterior at $k^B_{\rm max} = 0.23\,h\,{\rm Mpc}^{-1}$ and $k^B_{\rm max} = 0.19\,h\,{\rm Mpc}^{-1}$. In addition, we see that parameters the $b_{\mathcal{G}_2}$ and b_{Γ_3} become biased. The optimal values of these parameters scale along the degeneracy direction $b_{\mathcal{G}_2} + 0.34 b_{\Gamma_3} \approx$ const, which closely matches the degeneracy combination imposed by the power spectrum, $b_{\mathcal{G}_2} + 0.4 b_{\Gamma_3}$ [11].

TABLE I. One-dimensional marginalized contraints on low-order bias parameters and the clustering amplitude σ_8 extracted from the PT Challenge dataset. We display results obtained using only the power spectrum multipoles P_ℓ (left panel, cf. [100]), and those including the power spectrum, Q_0 and the one-loop real-space bispectrum likelihood with $k^B_{\rm max} = 0.21\,h\,{\rm Mpc}^{-1}$ (right panel). The one-loop bispectrum is the main new feature of this work. Most parameters are normalized to their true values, to avoid unblinding the simulation. In real space, the addition of the bispectrum significantly tightens posteriors on bias parameters (by at least an order of magnitude), and gives ≈20% improvement on σ_8. Further details are given in the main text, with corresponding results for the redshift-space bispectrum shown in Table II.

P_ℓ	
Parameter	68% limits
$\Delta\sigma_8/\sigma_8$	0.0080 ± 0.0064
$\Delta(b_1\sigma_8)/(b_1\sigma_8)$	$-0.0063^{+0.0042}_{-0.0038}$
Δb_2	$-0.04^{+0.44}_{-0.56}$
$\Delta b_{\mathcal{G}_2}$	$0.08^{+0.25}_{-0.34}$
Δb_{Γ_3}	⋯

$P_\ell + Q_0 + B_{\rm real}$	
Parameter	68% limits
$\Delta\sigma_8/\sigma_8$	0.0005 ± 0.0049
$\Delta(b_1\sigma_8)/(b_1\sigma_8)$	-0.0003 ± 0.0013
Δb_2	-0.005 ± 0.037
$\Delta b_{\mathcal{G}_2}$	-0.003 ± 0.017
Δb_{Γ_3}	0.005 ± 0.050

In contrast with the $k^B_{\rm max} \geq 0.21\,h{\rm Mpc}^{-1}$ picture, the results at all choices of $k^B_{\rm max} \leq 0.21\,h{\rm Mpc}^{-1}$ are fully consistent, implying that $k^B_{\rm max} = 0.21\,h\,{\rm Mpc}^{-1}$ should be chosen as a baseline scale cut. This is somewhat larger than the one-loop power spectrum scale cut of $k_{\rm max} = 0.16\,h\,{\rm Mpc}^{-1}$; whilst this might appear unusual, we note that the power spectrum contains a significantly higher signal-to-noise ratio, and is subject to redshift-space complexities, both of which decrease $k^P_{\rm max}$. We use best-fit values of nuisance parameters from the baseline $P_\ell + Q_0 + B(k^B_{\rm max} = 0.21\,h\,{\rm Mpc}^{-1})$ analysis as ground truth values in the below.

It is instructive to compare the parameter constraints extracted using the one-loop bispectrum to those from the power spectrum multipoles alone, i.e., $P_\ell(k)$ at the baseline $k_{\rm max} = 0.16\,h\,{\rm Mpc}^{-1}$. These are shown in the left panel of Table I. We find an improvement of 31% in σ_8, whilst the error bars on bias parameters tighten by an order of magnitude in some cases. Despite the noticeable increase in signal-to-noise ratio of the dataset, we find a modest improvement in σ_8: this is linked to the proliferation of bias, counterterm, and stochasticity parameters needed to describe the one-loop bispectrum in an unbiased manner.

It is also useful to compare our one-loop bispectrum results with those from the tree-level bispectrum. We cannot directly use results from [80] since the former work also varied other cosmological parameters such as H_0 and Ω_m. To obtain a cleaner comparison, we repeat the tree-level analysis of [80] with the same analysis settings as here, using $k^B_{\rm max} = 0.08\,h\,{\rm Mpc}^{-1}$ for the tree-level bispectrum. We find $\Delta\sigma_8/\sigma_8 = 0.002 \pm 0.0053$, i.e., an 21% improvement over the power spectrum only result. Comparing this the present analysis, we see that the addition of the one-loop bispectrum likelihood yields an extra 10% improvement over the tree-level bispectrum likelihood.

Finally, we compare our results with those of [81]. Unlike our work, [81] used the power spectrum of halos and galaxies in real space, leading to the notorious $b_1 - \sigma_8$ degeneracy being largely unbroken. This explains why our results on σ_8 are much better—most of the constraining power comes from redshift-space distortions omitted in [81]. Despite this difference, our analysis does confirm a general trend pointed out in [81]—the returns from the one-loop bispectrum are limited by the large number of nuisance parameters. As such, it will be important to obtain better priors on them in the future, for example using hydrodynamical simulations.

B. Primordial non-Gaussianity

It is interesting to study to what extent the one-loop bispectrum model can help improve constraints on primordial non-Gaussianity (PNG), following constraints from the tree-level bispectrum in [96,97]. We consider here the case of equilateral PNG, which induces the following three-point correlation of the linear density field (see [96] for further details),

$$\langle \delta^{(1)}_{\mathbf{k}_1}\delta^{(1)}_{\mathbf{k}_2}\delta^{(1)}_{\mathbf{k}_3}\rangle = (2\pi)^3\delta^{(3)}_D(\mathbf{k}_{123})B_{\rm equil}(k_1,k_2,k_3),$$
$$B_{\rm equil} = \prod_{a=1}^{3} T(k_a)\left[\frac{18}{5}f^{\rm equil}_{\rm NL}\Delta^4_\zeta\frac{\mathcal{S}_{\rm equil}(k_1,k_2,k_3)}{k_1^2k_2^2k_3^2}\right],$$
$$\mathcal{S}_{\rm equil}(k_1,k_2,k_3) = \left(\frac{k_1}{k_2}+5\,{\rm perms.}\right) - \left(\frac{k_1^2}{k_2k_3}+2\,{\rm perms.}\right) - 2, \tag{5.1}$$

where ζ is the primordial curvature fluctuation with dimensionless amplitude Δ_ζ, and we have introduced the transfer function $T(k) = (P_{11}(k)/P_\zeta(k))^{1/2}$.

Non-Gaussianity in the initial conditions generates three main effects [96]: (1) an additional contribution B_{111} to the tree-level bispectrum, (2) an extra one-loop power spectrum correction P_{12}, and (3) further contributions in the galaxy bias expansion, which modifies the tree-level expressions

by introducing the so-called scale-dependent bias. The latter stems from the following expression:

$$\delta_g \subset b_\zeta \nabla^2 \zeta + \cdots, \tag{5.2}$$

where "..." denote nonlinear PNG corrections which can be ignored for the purposes of this paper. The term $\nabla^2\zeta$ generates tree-level "scale-dependent" bias corrections to the power spectrum. Note that these corrections are suppressed in the equilateral case with respect to the case of local PNG, where the scale-dependent bias is a leading effect on the galaxy power spectrum, and thus the power spectrum dominates the constraining power on $f_{\rm NL}^{\rm loc}$.

As shown in [96], for the one-loop power spectrum and tree-level bispectrum, we must include all three of the P_{12}, B_{111}, and b_ζ-related terms in our model. In this paper, we consider the one-loop bispectrum, which technically requires additional nonlinear $f_{\rm NL}^{\rm equil}$ corrections to the galaxy bispectrum, such as $B_{113}^{(I)}$, $B_{113}^{(II)}$, $B_{122}^{(I)}$, $B_{113}^{(II)}$ [111,129]. However, given that $f_{\rm NL}^{\rm eq}\Delta_\zeta$ is small, these will be suppressed, thus we leave their systematic calculation for future work, focusing only on the leading terms, similar to [96,98]. For $f_{\rm NL}^{\rm equil} \lesssim 500$, the next-to-leading order contributions are subdominant to two-loop matter corrections for $k \lesssim 0.2\,h\,{\rm Mpc}^{-1}$.

Concerning scale cuts, we find that use of the P_ℓ and Q_0 statistics at high $k_{\rm max}$ can lead to biases in the recovered values of $f_{\rm NL}^{\rm equil}$. This is consistent with the estimates of [96], which showed that the two-loop corrections can actually be larger than the non-Gaussian P_{12} contribution at small scales. Thus, we choose $k_{\rm max} = 0.2\,h\,{\rm Mpc}^{-1}$ for the Q_0 statistics and $k_{\rm max} = 0.14\,h\,{\rm Mpc}^{-1}$ for P_ℓ in the PNG analysis of this section. For $B_{\rm real}$ we use the baseline data cut $k_{\rm max}^B = 0.21\,h\,{\rm Mpc}^{-1}$, motivated by the discussion above.

To perform the analyses including PNG, we fit the parameter $f_{\rm NL}^{\rm equil}$ in addition to σ_8 and nuisance parameters. Since the PT challenge simulations were run using purely Gaussian initial conditions, we expect to find $f_{\rm NL}^{\rm equil}$ consistent with zero. Indeed, our nominal constraint on the amplitude of the equilateral shape is given by

$$\text{1-loop}(k_{\rm max}^B = 0.21\,h\,{\rm Mpc}^{-1}):\, f_{\rm NL}^{\rm equil} = 72 \pm 80 (95\%\ \text{C.L.}). \tag{5.3}$$

We stress that these results are obtained without any external priors on σ_8 or the nonlinear bias coefficients. This constraint can be compared with that obtained from the tree-level real-space bispectrum likelihood,

$$\text{tree}(k_{\rm max}^B = 0.08\,h\,{\rm Mpc}^{-1}):\, f_{\rm NL}^{\rm equil} = 53 \pm 114 (95\%\ \text{C.L.}). \tag{5.4}$$

At face value, our results imply that the addition of the one-loop bispectrum can improve constraints on $f_{\rm NL}^{\rm equil}$ by $\sim$30%.

VI. RESULTS: REDSHIFT SPACE

In this section we present the analysis of the data vector $[P_\ell(k), Q_0(k), B_0(k_1, k_2, k_3)]$, where all statistics are in redshift space and include projection and coordinate-distortion effects. This setup thus fully matches an analysis of a realistic galaxy survey such as BOSS [2]. As for the power spectrum, we expect that the addition of redshift-space distortions (particularly the fingers-of-God effect [123], hereafter FOG), will reduce the nonlinear scale, thus it is likely that $k_{\rm max}^B$, and the constraining power of the bispectrum monopoole, will decrease.

A. Clustering amplitude and bias parameters

Let us discuss the recovery of the mass clustering amplitude σ_8 and bias parameters. As a point of comparison, we fix the fiducial bias parameters to those extracted from the real space analysis before with $k_{\rm max}^B = 0.21\,h\,{\rm Mpc}^{-1}$. We fit the redshift-space bispectrum data for the following choices of scale cuts:

$$k_{\rm max}^B/(h\,{\rm Mpc}^{-1}) = 0.15, 0.17, 0.20, 0.22. \tag{6.1}$$

The resulting posterior contours are shown in Fig. 3, and we observe that all parameters of interest are unbiased at $k_{\rm max}^B = 0.15\,h\,{\rm Mpc}^{-1}$. For comparison, we also show the baseline real space bispectrum results of § V. Note that if we use $k_{\rm max}^B < 0.15\,h\,{\rm Mpc}^{-1}$, the bispectrum data is not sufficient to constrain all the nuisance parameters entering the theory model. This gives rise to significant marginalization projection effects, which can be naïvely interpreted as a bias in our model. We study these effects in Appendix E and show that the measurements at $k_{\rm max}^B < 0.15\,h\,{\rm Mpc}^{-1}$ are consistent with our baseline choice $k_{\rm max}^B = 0.15\,h\,{\rm Mpc}^{-1}$ once projection effects are taken into account.

At $k_{\rm max}^B = 0.17\,h\,{\rm Mpc}^{-1}$ the clustering amplitude σ_8, the rescaled linear bias $b_1\sigma_8$, b_2 and b_{Γ_3} become biased with respect to their optimal values coming from the real-space bispectrum analysis. These biases are accompanied with a significant increase in the χ^2 statistics. Thus, we conclude that the two-loop bispectrum corrections are not negligible at this scale. This is further supported by the bias growing with $k_{\rm max}^B$: in particular, at $k_{\rm max}^B = 0.22\,h$ Mpc^{-1} the bias on σ_8 reaches 2%, which is significant in the context of the PT Challenge simulation volume. In conclusion, we find that the one-loop galaxy bispectrum model in redshift space works well up to $k_{\rm max}^B = 0.15\,h\,{\rm Mpc}^{-1}$ for the precision that corresponds to the total volume of the PT Challenge simulation (which we recall is significantly larger than

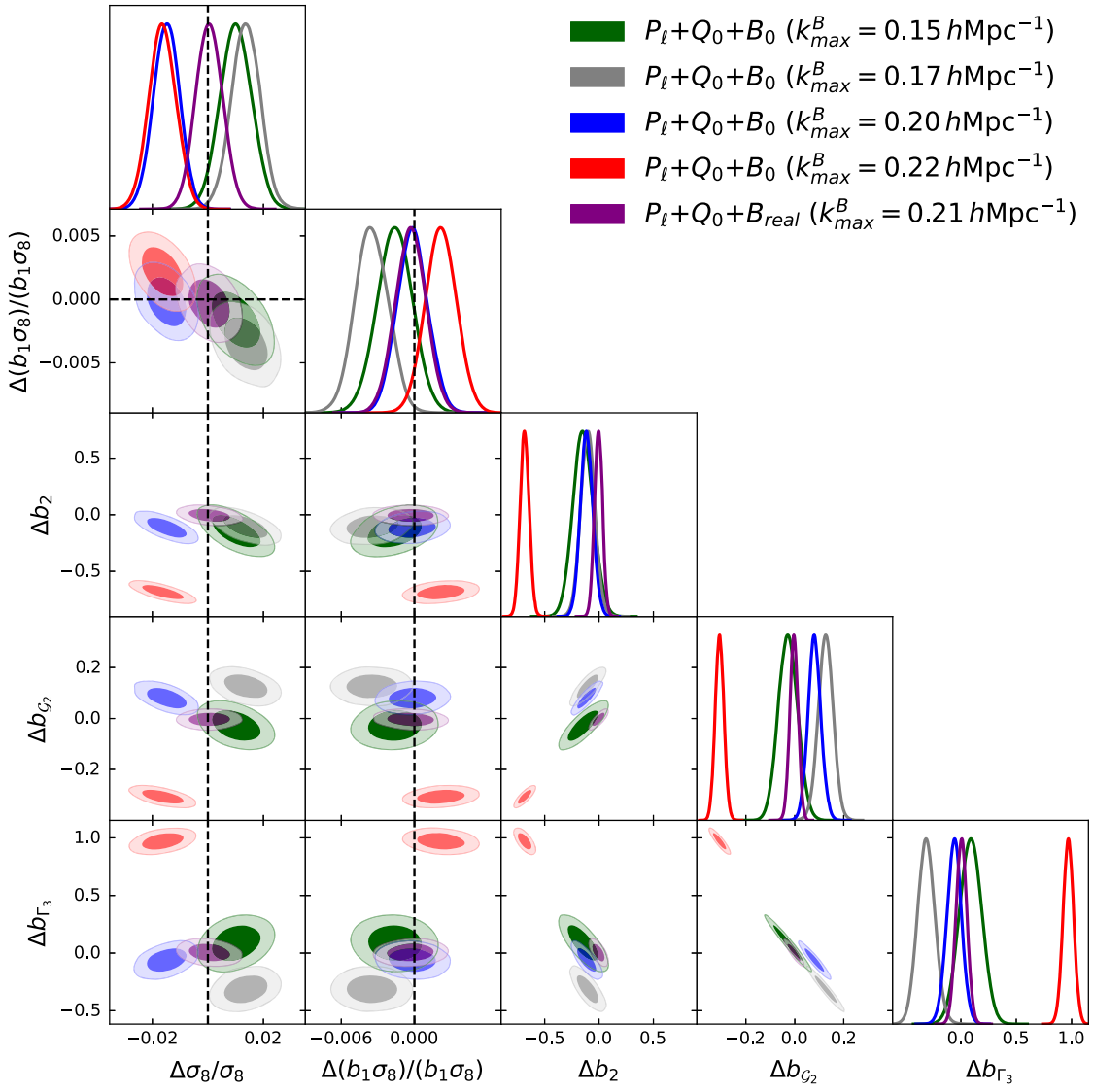

FIG. 3. Posterior distributions of the clustering amplitude and certain nuisance parameters obtained from MCMC analyses of the power spectra and one-loop redshift-space bispectrum monopole B_0. The power spectrum likelihood is the same for all cases. We show results for different values of the bispectrum data cut $k^B_{\rm max}$, as indicated by the caption. This is analogous to Fig. 2 (whose optimal constraint is shown by the purple curve), but utilizes the redshift-space bispectrum. Corresponding marginalized parameter constraints with $k^B_{\rm max} = 0.15\,h\,{\rm Mpc}^{-1}$ are given in Table II.

current and forthcoming datasets). The optimal values of cosmological and bias parameters for this choice are presented in Table II. For comparison, we also show the results from the tree-level bispectrum analysis akin to [80].[9] That $k^B_{\rm max}$ is lower in redshift space than real space is no surprise: this indicates that the characteristic scale of FOG effects ($\sigma_{\rm FOG}$) is smaller than that of nonlinearities ($k^{-1}_{\rm NL}$). For the power spectrum in redshift-space, higher-order counterterms were important to model FOG, scaling as k^4_z. An analogous set of nuisance parameters may be included here, but we caution that their number is large due to the higher dimensionality of the bispectrum.

Considering the marginalized posteriors directly, we find that the one-loop bispectrum likelihood (at $k^B_{\rm max}=0.15h{\rm Mpc}^{-1}$) yields only a 12% improvement on σ_8 compared to the power spectrum alone, though the

[9]For this analysis we use $k^B_{\rm max} = 0.06\,h\,{\rm Mpc}^{-1}$ and set the c_1 counterterm to zero for consistency with our one-loop model. This term served as a proxy for the one-loop corrections; thus its inclusion is equivalent to partially accounting for one-loop information. To clearly compare the tree-level and one-loop results, we exclude it here.

TABLE II. One-dimensional marginalized constraints on low-order bias parameters and the clustering amplitude σ_8 extracted from the PT Challenge dataset. We show the fit from the combined likelihood including power spectrum multipoles, Q_0, the tree-level redshift-space bispectrum at $k^B_{\rm max} = 0.06\,h\,{\rm Mpc}^{-1}$ (left table) and the one-loop redshift-space bispectrum at $k^B_{\rm max} = 0.15\,h\,{\rm Mpc}^{-1}$ (right table). The parameters are normalized relative to their true values. Whilst we find significant enhancements in the bias parameter constraints compared to the power spectrum alone (cf. Table I), the constraint on σ_8 does not improve appreciably.

$P_\ell + Q_0 + B_0^{\rm tree}$	
Parameter	68% limits
$\Delta\sigma_8/\sigma_8$	0.0003 ± 0.0054
$\Delta(b_1\sigma_8)/(b_1\sigma_8)$	-0.0025 ± 0.0016
Δb_2	-0.085 ± 0.082
$\Delta b_{\mathcal{G}_2}$	0.034 ± 0.046
Δb_{Γ_3}	-0.12 ± 0.12

$P_\ell + Q_0 + B_0^{\rm 1-loop}$	
Parameter	68% limits
$\Delta\sigma_8/\sigma_8$	0.0101 ± 0.0057
$\Delta(b_1\sigma_8)/(b_1\sigma_8)$	-0.0016 ± 0.0015
Δb_2	-0.146 ± 0.094
$\Delta b_{\mathcal{G}_2}$	-0.028 ± 0.039
Δb_{Γ_3}	0.09 ± 0.10

constraints on bias parameters (and thus astrophysics) improve markedly. Comparing this with the tree-level case, we see that the inclusion of one-loop corrections actually lead to a somewhat worse result than for tree-level bispectrum, which tightens the σ_8 constraint by 18% for the analysis settings adopted in this work. This is consistent with previous studies considering the real-space bispectrum [81], and arises primarily due to the large number of nuisance parameters appearing in the one-loop calculation, especially in redshift space. A similar situation takes place in the context of the one-loop redshift-space power spectrum, whose information content is limited by marginalization over nuisance parameters [24]. We will discuss this issue in detail later.

VII. IMPLICATIONS FOR THE BOSS SURVEY

In this section we estimate the potential performance of the one-loop bispectrum model applied to the BOSS survey data [2], which is the largest publicly available spectroscopic galaxy clustering dataset. This survey has significantly smaller volume than our mock simulation data, so one can expect that the analysis can be pushed to smaller scales [16,80]. Indeed, the relevant parameter in this problem is the ratio of the theory systematic bias in a certain parameter to the statistical error on that parameter. For the BOSS volume the statistical errors are significantly larger than the PT Challenge simulation volume, due to a ratio of volumes of ≈100. As the theoretical errors do not depend on the volume, the ratio between the theoretical error and statistical errors thus becomes smaller, and hence any residual theoretical systematics becomes less sizable in relative terms.

To demonstrate this, we repeat the likelihood analysis above for the redshift-space data vector $[P_\ell, Q_0, B_0]$, but rescale the covariance to match the BOSS volume $V_{\rm BOSS} = V_{\rm PT\,Challenge}/100 \simeq 6\,(h^{-1}\,{\rm Gpc})^3$. We select $k_{\rm max} = 0.20\,h\,{\rm Mpc}^{-1}$ for power spectrum multipoles P_ℓ and $k^B_{\rm max} = 0.20\,h\,{\rm Mpc}^{-1}$ for the bispectrum monopole B_0; significantly larger than that found in §VI. The results of this analysis are presented in Fig. 4 and in Table III, showing also the $P_\ell + Q_0$ and $P_\ell + Q_0 + B_0^{\rm tree}$ ($k^B_{\rm max} = 0.08\,h\,{\rm Mpc}^{-1}$ following [80]) analyses for comparison.

We see that in the context of BOSS, the addition of the one-loop bispectrum yields an ≈24% improvement over the power spectrum-only result and an ≈10% improvement over the tree-level bispectrum likelihood result. However, this leads to a noticeable shift in nuisance parameters, with $b_{\mathcal{G}_2}$ approximately 1.7σ from its fiducial value. This could simply be a prior-volume effect however (since the effect of the priors becomes more important at lower simulation volume), especially given that $b_{\mathcal{G}_2}$ departs from its fiducial value at 1.1σ already for the power-spectrum alone. The tree-level bispectrum analysis, however, results in an unbiased recovery of all nuisance and cosmological parameters.

It is also instructive to study whether the one-loop bispectrum can improve constraints on equilateral PNG. Incorporating this parameter in the analysis as before (varying both $f_{\rm NL}^{\rm equil}$ and σ_8) we find $f_{\rm NL}^{\rm equil} = 197 \pm 350$. For the clustering amplitude we find $\Delta\sigma_8/\sigma_8 = -0.026 \pm 0.035$, with a slight 0.6σ shift with respect to the ground truth. For comparison, we have also run an analysis using the tree-level bispectrum at $k^B_{\rm max} = 0.08\,h\,{\rm Mpc}^{-1}$ instead of the one-loop bispectrum, and found $f_{\rm NL}^{\rm equil} = 420 \pm 440$, $\Delta\sigma_8/\sigma_8 = -0.025 \pm 0.040$. First, we see some bias in $f_{\rm NL}^{\rm equil}$, which can be attributed to prior volume effects and somewhat more optimistic data cuts for the power spectrum that we use in our analysis here. Indeed, in [96] it was shown that the tree-level model yields unbiased results on $f_{\rm NL}^{\rm equil}$ for $k^B_{\rm max} = 0.08\,h\,{\rm Mpc}^{-1}$ and $k^{P_\ell}_{\rm max} = 0.17\,h\,{\rm Mpc}^{-1}$. Second, we notice that the bound on $f_{\rm NL}^{\rm equil}$ in the one-loop case is 30% better than that of the tree-level analysis. The improvement is quite modest as a consequence of the

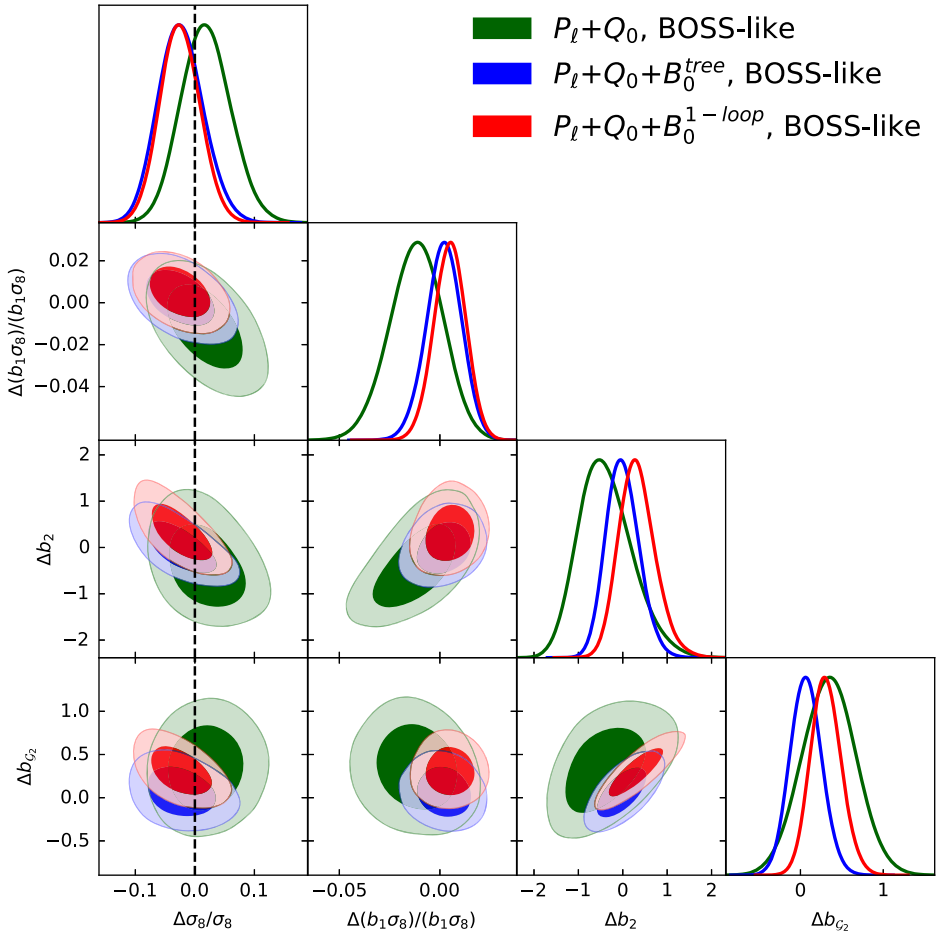

FIG. 4. Posterior distributions of the clustering amplitude and low-order nuisance parameters from MCMC analyses of the power spectrum data ($P_\ell + Q_0$, in green), and the combination of the power spectrum and redshift-space bispectrum monopole ($P_\ell + Q_0 + B_0$), using tree-level (blue, from [80]) and one-loop (red) theories. The covariance is rescaled to match the volume of the BOSS survey, and we assume $k_{\rm max} = 0.2\ h^{-1}$ Mpc for both the one-loop power spectrum and bispectrum.

fact that the one-loop model introduces many nuisance parameters, which cannot be constrained by the data. In our analysis we use highly conservative but still physically motivated priors; if more aggressive priors on nuisance parameters are used, the constraints are likely to improve further.

In conclusion, we note that the addition of the one-loop bispectrum may yield some ≈30% improvement on the amplitude of equilateral PNG. We stress, however, that this comes with two important caveats. First, the $k^B_{\rm max}$ used for this study ($0.2\,h\,{\rm Mpc}^{-1}$) results in noticeable biases on the nuisance parameters, suggesting that the error bar on $f_{\rm NL}^{\rm equil}$ may be underestimated due to overfitting. Whether this induces a bias on $f_{\rm NL}^{\rm equil}$ is unclear; such an error would likely show up only in the analysis of simulations containing $f_{\rm NL}^{\rm equil} \neq 0$. Second, we have neglected the PNG-induced one-loop corrections to the bispectrum (as in [98]), which can be marginally important for the scales of interest (particularly in the tails of the $f_{\rm NL}^{\rm equil}$ posterior), as can be easily estimated with the scaling universe approximation outlined in [129].

Finally, we note that our analysis indicates a more modest improvement on $f_{\rm NL}^{\rm equil}$ than that reported in [98]. Reference [98] suggest that the one-loop bispectrum improves $f_{\rm NL}^{\rm equil}$ constraints over the tree-level result by a factor of few. This follows from a comparison with the tree-level bispectrum analysis of [96]. This comparison is misleading, however, since the baseline analysis of [96] varies cosmology whilst [98] always keeps cosmological parameters fixed. We have checked that this accounts for most of the difference between [96,98]. A more detailed comparison with [98] is not currently possible because the former work has not yet presented sufficient details about their analysis and theory model. It will be interesting to compare our results with their analysis in the future.

TABLE III. One-dimensional marginalized constraints on low-order bias parameters and the clustering amplitude σ_8 extracted from the PT Challenge dataset, with covariance adjusted to match the volume of the BOSS survey. We show results for the $P_\ell + Q_0$ only analysis (top left), the tree-level $P_\ell + Q_0 + B_0$ likelihood (top right), and the one-loop $P_\ell + Q_0 + B_0$ likelihood (bottom). The inclusion of the bispectrum sharpens constraints on σ_8 by ≈24%, with some ≈10% improvement arising from the addition of the one-loop contributions.

$P_\ell + Q_0$, BOSS-like	
Parameter	68% limits
$\Delta\sigma_8/\sigma_8$	0.019 ± 0.042
$\Delta(b_1\sigma_8)/(b_1\sigma_8)$	-0.013 ± 0.013
Δb_2	$-0.37^{+0.50}_{-0.68}$
$\Delta b_{\mathcal{G}_2}$	0.37 ± 0.33

$P_\ell + Q_0 + B_0^{\rm tree}$, BOSS-like	
Parameter	68% limits
$\Delta\sigma_8/\sigma_8$	$-0.023^{+0.035}_{-0.040}$
$\Delta(b_1\sigma_8)/(b_1\sigma_8)$	0.0021 ± 0.0089
Δb_2	$-0.02^{+0.34}_{-0.40}$
$\Delta b_{\mathcal{G}_2}$	0.07 ± 0.19

$P_\ell + Q_0 + B_0^{\rm 1-loop}$, BOSS-like	
Parameter	68% limits
$\Delta\sigma_8/\sigma_8$	-0.025 ± 0.034
$\Delta(b_1\sigma_8)/(b_1\sigma_8)$	0.0051 ± 0.0080
Δb_2	$0.31^{+0.35}_{-0.45}$
$\Delta b_{\mathcal{G}_2}$	$0.31^{+0.17}_{-0.19}$

VIII. CONCLUSIONS AND DISCUSSION

In this work, we have presented and validated a complete calculation of the galaxy bispectrum monopole in redshift space at one-loop order in effective field theory. Our model includes one-loop corrections due to mode coupling, as well as the full set of EFT counterterms that are needed to regulate the UV behavior of loop integrals and capture the physical effects of backreaction of short scales onto the large-scale modes. Furthermore, we incorporate a bias expansion up to fourth order (noting that many operators vanish after renormalization of the power spectrum and bispectrum) as well as fourth order redshift-space distortions. In addition, our calculation includes IR resummation to capture the nonlinear evolution of baryon acoustic oscillations (both for the power spectrum and bispectrum), as well as projection and binning effects. In short, we include all relevant ingredients needed to compare theory with observational galaxy clustering data.

We have studied the performance of the one-loop bispectrum model in terms of cosmological parameter constraints, focusing primarily on the mass fluctuation amplitude σ_8. To validate our model we use the PT Challenge simulation suite [100], which are equivalent to a BOSS-like survey with a hundred times larger volume, thus allowing for high-precision tests. We analyze a data vector that consists of the standard redshift-space power spectrum multipoles, the real-space power spectrum proxy Q_0 [121], and the redshift-space bispectrum monopole. In this setup, we have found that the inclusion of the one-loop corrections allows us to extend the agreement between bispectrum theory and data up to $k_{\rm max} = 0.15\,h\,{\rm Mpc}^{-1}$, or $k_{\rm max} = 0.21\,h\,{\rm Mpc}^{-1}$ in real space. This can be contrasted with the tree-level model bispectrum model, which works only up to $k_{\rm max} = 0.08\,h\,{\rm Mpc}^{-1}$ [80]. We caution that these scale cuts depend on both the survey volume and galaxy type: for BOSS, we can use $k_{\rm max} = 0.20\,h\,{\rm Mpc}^{-1}$, and it is likely that the wave number reach is larger for emission line galaxies, which boast smaller FOG effects [12,64]. Further, one might hope to extend the k reach by specializing to some real-space bispectrum analog (similar to Q_0) at high k: this will be considered in future work.

Despite a significant extension of the k-space reach, we have not found the bispectrum to lead to noticeable improvements in the σ_8 constraints compared to those with obtained from tree-level theory when applied to the PT Challenge simulations. This is a consequence of the large number of the EFT nuisance parameters that appear in the one-loop calculation (particularly in redshift space), and must be marginalized over in our analysis. For a BOSS-volume survey (and accompanying systematic error thresholds), we find greater utility, with the one-loop bispectrum improving constraints by ∼10% over the tree-level case, though it remains to be seen whether any accompanying shifts in nuisance parameters are real (and malignant) or just prior volume effects.

We have additionally studied whether the one-loop bispectrum can help constrain equilateral primordial non-Gaussianity (and thus single-field inflation), finding that, for the BOSS survey, the one-loop bispectrum may improve constraints on the non-Gaussianity parameter $f_{\rm NL}^{\rm equil}$ by ≈30% compared to the tree-level theory. Achieving this, however, requires pushing the bispectrum analysis to $k_{\rm max}^B = 0.2h{\rm Mpc}^{-1}$, where the shifts in the bias parameters become evident. It remains to be seen if this problem can be alleviated with better priors on nuisance parameters or with one-loop PNG-induced corrections to the bispectrum, which were omitted in this study. If one is interested in astrophysics, the one-loop bispectrum is much more useful: we find a significant tightening in the posteriors of parameters such as linear and tidal bias compared to those with only tree-level theory.

An important conclusion from our study is that we need better knowledge of the EFT nuisance parameters if we wish to extract more cosmological information from the bispectrum. This can be done in several ways. First, one can include data from the higher-order angular moments of the redshift-space bispectrum [37]. Since these moments depend on the same set of parameters, their inclusion should tighten the EFT nuisance parameters posteriors, aiding

determination of the cosmological parameters of interest. Second, one can constrain the EFT nuisance parameters with higher order statistics, such as the trispectrum, see, e.g., [102,130] for work in this direction. Finally, one can obtain better priors on the extra nuisance parameters using high fidelity N-body or hydrodynamical simulations. A powerful route by which to achieve this involves EFT field level techniques, see, e.g., [85,119,131–138]. We plan to investigate these options in future work.

Though the one-loop bispectrum analysis of this work was limited only to two cosmological parameters, the mass fluctuation amplitude and the equilateral non-Gaussianity parameter, it may be similarly extended to other parameters such as local primordial non-Gaussianity, or the neutrino mass. The improvement on other parameters, especially those beyond the minimal ΛCDM model, could be significantly larger, particularly when some new feature is introduced that is not degenerate with the smooth loop corrections. If the parameter of interest enters the theoretical model linearly, the analysis can proceed as above; if this is not the case, one would require an optimization of our one-loop bispectrum pipeline, since the FFTLog-based approach does not currently allow for a fast recalculation of the theoretical template as the power spectrum is varied. If only the $\alpha_\parallel, \alpha_\perp$ parameters are varied however, then the templates do not need to be recomputed, only rebinned (via (2.21). Analyses including such effects will be natural next steps in our research program.

Finally, we note that the bispectrum data offers novel probes of new physics. In particular, constructing the bispectrum from different tracers will allow one to probe the equivalence principle [53–59]. Such an analysis is complicated if one considers only the power spectrum since the effects sensitive to the equivalence principle appear there only at the one-loop order. In contrast, the cross-bispectrum of different kinds of tracers can be a sensible probe of the equivalence principle, whose violation would generate new bispectrum shapes that are not present in the ΛCDM (cold dark matter) model. This, in particular, will help one derive new constraints on the violation of Lorentz symmetry in the dark matter sector [139,140]. We leave this and other tests of new physics with the bispectrum for future work.

ACKNOWLEDGMENTS

We would like to thank Emanuele Castorina, Azadeh Moradinezhad Dizgah, and Zvonimir Vlah for useful discussions. O. H. E. P. thanks the Simons Foundation for support and acknowledges the Institute for Advanced Study for their hospitality and abundance of baked goods. The work of M. M. I. has been supported by NASA through the NASA Hubble Fellowship Grant No. HST-HF2-51483.001-A awarded by the Space Telescope Science Institute, which is operated by the Association of Universities for Research in Astronomy, Incorporated, under NASA Contract No. NAS5-26555. G. C. acknowledges support from the Institute for Advanced Study. M. Z. is supported by the Canadian Institute for Advanced Research (CIFAR) program on Gravity and the Extreme Universe and the Simons Foundation Modern Inflationary Cosmology initiative. This work was supported in part by MEXT/JSPS KAKENHI Grants No. JP19H00677, No. JP20H05861, No. JP21H01081, and No. JP22K03634. We also acknowledge financial support from Japan Science and Technology Agency (JST) AIP Acceleration Research Grant No. JP20317829. The simulation data analysis was performed partly on Cray XC50 at Center for Computational Astrophysics, National Astronomical Observatory of Japan. Data analysis was primarily performed on the Helios cluster at the Institute for Advanced Study, Princeton, and additional computations were carried out using the Princeton Research Computing resources at Princeton University, which is a consortium of groups led by the Princeton Institute for Computational Science and Engineering (PICSciE) and the Office of Information Technology's Research Computing Division.

APPENDIX A: PERTURBATION THEORY KERNALS

1. Real space

At fourth order, the real-space perturbation theory kernels [cf. (2.6)] are given by

$$
\begin{aligned}
K_1(\boldsymbol{q}_1) &= b_1,\\
K_2(\boldsymbol{q}_1,\boldsymbol{q}_2) &= \{b_1 F_2(\boldsymbol{q}_1,\boldsymbol{q}_2)\} + \left\{\frac{b_2}{2} + \gamma_2\kappa(\boldsymbol{q}_1,\boldsymbol{q}_2)\right\},\\
K_3(\boldsymbol{q}_1,\boldsymbol{q}_2,\boldsymbol{q}_3) &= \{b_1 F_3(\boldsymbol{q}_1,\boldsymbol{q}_2,\boldsymbol{q}_3)\} + \{b_2 F_2(\boldsymbol{q}_1,\boldsymbol{q}_2) + 2\gamma_2\kappa(\boldsymbol{q}_1,\boldsymbol{q}_{23})G_2(\boldsymbol{q}_2,\boldsymbol{q}_3)\}\\
&\quad + \left\{\frac{b_3}{6} + \gamma_2^{\times}\kappa(\boldsymbol{q}_1,\boldsymbol{q}_2) + \gamma_3 L(\boldsymbol{q}_1,\boldsymbol{q}_2,\boldsymbol{q}_3) + \gamma_{21}\kappa(\boldsymbol{q}_1,\boldsymbol{q}_{23})\kappa(\boldsymbol{q}_2,\boldsymbol{q}_3)\right\},\\
K_4(\boldsymbol{q}_1,\boldsymbol{q}_2,\boldsymbol{q}_3,\boldsymbol{q}_4) &= \{b_1 F_4(\boldsymbol{q}_1,\boldsymbol{q}_2,\boldsymbol{q}_3,\boldsymbol{q}_4)\} + \left\{\frac{b_2}{2}[F_2(\boldsymbol{q}_1,\boldsymbol{q}_2)F_2(\boldsymbol{q}_3,\boldsymbol{q}_4) + 2F_3(\boldsymbol{q}_1,\boldsymbol{q}_2,\boldsymbol{q}_3)]\right.\\
&\quad \left. + \gamma_2[\kappa(\boldsymbol{q}_{12},\boldsymbol{q}_{34})G_2(\boldsymbol{q}_1,\boldsymbol{q}_2)G_2(\boldsymbol{q}_3,\boldsymbol{q}_4) + 2\kappa(\boldsymbol{q}_{123},\boldsymbol{q}_4)G_3(\boldsymbol{q}_1,\boldsymbol{q}_2,\boldsymbol{q}_3)]\right\}
\end{aligned}
$$

$$
\begin{aligned}
&+\left\{\frac{b_3}{2}F_2(\boldsymbol{q}_1,\boldsymbol{q}_2)+\gamma_2^{\times}[2\kappa(\boldsymbol{q}_{12},\boldsymbol{q}_3)G_2(\boldsymbol{q}_1,\boldsymbol{q}_2)+\kappa(\boldsymbol{q}_3,\boldsymbol{q}_4)F_2(\boldsymbol{q}_1,\boldsymbol{q}_2)]+3\gamma_3 L(\boldsymbol{q}_1,\boldsymbol{q}_2,\boldsymbol{q}_{34})G_2(\boldsymbol{q}_3,\boldsymbol{q}_4)\right.\\
&\left.+\gamma_{21}[\kappa(\boldsymbol{q}_{12},\boldsymbol{q}_{34})\kappa(\boldsymbol{q}_1,\boldsymbol{q}_2)F_2(\boldsymbol{q}_3,\boldsymbol{q}_4)+2\kappa(\boldsymbol{q}_{123},\boldsymbol{q}_4)\kappa(\boldsymbol{q}_{12},\boldsymbol{q}_3)F_2(\boldsymbol{q}_1,\boldsymbol{q}_2)]\right\}\\
&+\left\{\gamma_{21}^{\times}\kappa(\boldsymbol{q}_1,\boldsymbol{q}_{23})\kappa(\boldsymbol{q}_2,\boldsymbol{q}_3)+\gamma_{211}L(\boldsymbol{q}_1,\boldsymbol{q}_2,\boldsymbol{q}_{34})\kappa(\boldsymbol{q}_3,\boldsymbol{q}_4)+\gamma_{22}\kappa(\boldsymbol{q}_{12},\boldsymbol{q}_{34})\kappa(\boldsymbol{q}_1,\boldsymbol{q}_2)\kappa(\boldsymbol{q}_3,\boldsymbol{q}_4)\right.\\
&+\gamma_{31}\left[\frac{1}{18}\kappa(\boldsymbol{q}_1,\boldsymbol{q}_{234})\left(\frac{15}{7}\kappa(\boldsymbol{q}_{23},\boldsymbol{q}_4)\kappa(\boldsymbol{q}_2,\boldsymbol{q}_3)-L(\boldsymbol{q}_2,\boldsymbol{q}_3,\boldsymbol{q}_4)\right)\right.\\
&\left.\left.+\frac{1}{14}(M(\boldsymbol{q}_1,\boldsymbol{q}_{23},\boldsymbol{q}_4,\boldsymbol{q}_{234})-M(\boldsymbol{q}_1,\boldsymbol{q}_{234},\boldsymbol{q}_{23},\boldsymbol{q}_4))\kappa(\boldsymbol{q}_2,\boldsymbol{q}_3)\right]\right\},
\end{aligned}
\tag{A1}
$$

where the bias parameters are shown in color, $\boldsymbol{q}_{i\cdots j}\equiv\boldsymbol{q}_i+\cdots+\boldsymbol{q}_j$ and we define the angles

$$
\begin{aligned}
\kappa(\boldsymbol{q}_1,\boldsymbol{q}_2)&=(\hat{\boldsymbol{q}}_1\cdot\hat{\boldsymbol{q}}_2)^2-1,\\
L(\boldsymbol{q}_1,\boldsymbol{q}_2,\boldsymbol{q}_3)&=2(\hat{\boldsymbol{q}}_1\cdot\hat{\boldsymbol{q}}_2)(\hat{\boldsymbol{q}}_2\cdot\hat{\boldsymbol{q}}_3)(\hat{\boldsymbol{q}}_3\cdot\hat{\boldsymbol{q}}_1)-(\hat{\boldsymbol{q}}_1\cdot\hat{\boldsymbol{q}}_2)^2-(\hat{\boldsymbol{q}}_2\cdot\hat{\boldsymbol{q}}_3)^2-(\hat{\boldsymbol{q}}_3\cdot\hat{\boldsymbol{q}}_1)^2+1,\\
M(\boldsymbol{q}_1,\boldsymbol{q}_2,\boldsymbol{q}_3,\boldsymbol{q}_4)&=(\hat{\boldsymbol{q}}_1\cdot\hat{\boldsymbol{q}}_2)(\hat{\boldsymbol{q}}_2\cdot\hat{\boldsymbol{q}}_3)(\hat{\boldsymbol{q}}_3\cdot\hat{\boldsymbol{q}}_4)(\hat{\boldsymbol{q}}_4\cdot\hat{\boldsymbol{q}}_1).
\end{aligned}
\tag{A2}
$$

Equation (A1) uses the standard Eulerian density and velocity kernels (F_n and G_n) and we note that the kernels have not been symmetrized over their arguments. We additionally note that, despite appearing in K_4, b_3 does not contribute to the one-loop bispectrum after averaging over internal angles and performing bias renormalization. Furthermore, we drop any bias operators in K_4 that do not appear in the one-loop bispectrum, thus the above expression will not be sufficient for computation of the two-loop power spectrum.

2. Redshift space

The redshift-space kernels are obtained by expanding the redshift space distortions (RSD) mapping of (2.7) and expanding all fields in terms of the linear density field. Following a lengthy computation, we find the following forms in terms of the real-space kernels:

$$
\begin{aligned}
Z_1(\boldsymbol{q}_1)&=K_1+f\mu_1^2,\\
Z_2(\boldsymbol{q}_1,\boldsymbol{q}_2)&=K_2(\boldsymbol{q}_1,\boldsymbol{q}_2)+f\mu_{12}^2G_2(\boldsymbol{q}_1,\boldsymbol{q}_2)+\frac{f\mu_{12}q_{12}}{2}K_1\left[\frac{\mu_1}{q_1}+\frac{\mu_2}{q_2}\right]+\frac{(f\mu_{12}q_{12})^2}{2}\frac{\mu_1}{q_1}\frac{\mu_2}{q_2},\\
Z_3(\boldsymbol{q}_1,\boldsymbol{q}_2,\boldsymbol{q}_3)&=K_3(\boldsymbol{q}_1,\boldsymbol{q}_2,\boldsymbol{q}_3)+f\mu_{123}^2G_3(\boldsymbol{q}_1,\boldsymbol{q}_2,\boldsymbol{q}_3)+(f\mu_{123}q_{123})\left[\frac{\mu_{12}}{q_{12}}K_1G_2(\boldsymbol{q}_1,\boldsymbol{q}_2)+\frac{\mu_3}{q_3}K_2(\boldsymbol{q}_1,\boldsymbol{q}_2)\right]\\
&\quad+\frac{(f\mu_{123}q_{123})^2}{2}\left[2\frac{\mu_{12}}{q_{12}}\frac{\mu_3}{q_3}G_2(\boldsymbol{q}_1,\boldsymbol{q}_2)+\frac{\mu_1}{q_1}\frac{\mu_2}{q_2}K_1\right]+\frac{(f\mu_{123}q_{123})^3}{6}\frac{\mu_1}{q_1}\frac{\mu_2}{q_2}\frac{\mu_3}{q_3},\\
Z_4(\boldsymbol{q}_1,\boldsymbol{q}_2,\boldsymbol{q}_3,\boldsymbol{q}_4)&=K_4(\boldsymbol{q}_1,\boldsymbol{q}_2,\boldsymbol{q}_3,\boldsymbol{q}_4)+f\mu_{1234}^2G_4(\boldsymbol{q}_1,\boldsymbol{q}_2,\boldsymbol{q}_3,\boldsymbol{q}_4)\\
&\quad+(f\mu_{1234}q_{1234})\left[\frac{\mu_{123}}{q_{123}}K_1G_3(\boldsymbol{q}_1,\boldsymbol{q}_2,\boldsymbol{q}_3)+\frac{\mu_4}{q_4}K_3(\boldsymbol{q}_1,\boldsymbol{q}_2,\boldsymbol{q}_3)+\frac{\mu_{12}}{q_{12}}G_2(\boldsymbol{q}_1,\boldsymbol{q}_2)K_2(\boldsymbol{q}_3,\boldsymbol{q}_4)\right]\\
&\quad+\frac{(f\mu_{1234}q_{1234})^2}{2}\left[2\frac{\mu_{123}}{q_{123}}\frac{\mu_4}{q_4}G_3(\boldsymbol{q}_1,\boldsymbol{q}_2,\boldsymbol{q}_3)+\frac{\mu_{12}}{q_{12}}\frac{\mu_{34}}{q_{34}}G_2(\boldsymbol{q}_1,\boldsymbol{q}_2)G_2(\boldsymbol{q}_3,\boldsymbol{q}_4)+2\frac{\mu_{12}}{q_{12}}\frac{\mu_3}{q_3}K_1G_2(\boldsymbol{q}_1,\boldsymbol{q}_2)\right.\\
&\quad\left.+\frac{\mu_1}{q_1}\frac{\mu_2}{q_2}K_2(\boldsymbol{q}_3,\boldsymbol{q}_4)\right]+\frac{(f\mu_{1234}q_{1234})^3}{6}\left[3\frac{\mu_{12}}{q_{12}}\frac{\mu_3}{q_3}\frac{\mu_4}{q_4}G_2(\boldsymbol{q}_1,\boldsymbol{q}_2)+\frac{\mu_1}{q_1}\frac{\mu_2}{q_2}\frac{\mu_3}{q_3}K_1\right]\\
&\quad+\frac{(f\mu_{1234}q_{1234})^4}{24}\frac{\mu_1}{q_1}\frac{\mu_2}{q_2}\frac{\mu_3}{q_3}\frac{\mu_4}{q_4},
\end{aligned}
\tag{A3}
$$

writing $\mu_{i\cdots j} \equiv \mu_{\boldsymbol{q}_i+\cdots+\boldsymbol{q}_j}$ and dropping the argument of K_1 for clarity.

APPENDIX B: COMPUTATION OF THE ONE-LOOP BISPECTRUM WITH FFTLOG

In this appendix, we discuss practical computation of the loop integrals given in (2.9). Before considering the redshift-space case, we will first examine how to compute the real-space integrals, which follow a similar logic, but are significantly simpler. Our approach follows [99], but is extended to the case of biased tracers and redshift space.

1. Real space

a. Formalism

As noted in § II, the first step in the bispectrum computation is the expansion of the perturbation theory kernels (Appendix A) as polynomials in q^2, $|\boldsymbol{k}_1-\boldsymbol{q}|^2$, and $|\boldsymbol{k}_2+\boldsymbol{q}|^2$ or their reciprocals (utilizing permutation symmetries). In practice, this results in a sum over many thousands of terms, once the relevant symmetries have been imposed, and is automated using *Mathematica*. For B_{222}, each term is proportional to

$$\int_{\boldsymbol{q}} \frac{P_L(q)P_L(|\boldsymbol{k}_1-\boldsymbol{q}|)P_L(|\boldsymbol{k}_2+\boldsymbol{q}|)}{q^{\alpha_1}|\boldsymbol{k}_1-\boldsymbol{q}|^{\alpha_2}|\boldsymbol{k}_2+\boldsymbol{q}|^{\alpha_3}}, \tag{B1}$$

for integer α_i, with a similar form found for the other loop integrals except with fewer factors of P_L. Expanding the linear power spectrum as a sum of complex polynomials in k, i.e., $P_L(k) = \sum_m c_m k^{\nu+i\eta_m}$ for frequencies η_m, coefficients c_m, and (real) FFTLog bias ν (which sets the eventual integral convergence properties), we can rewrite (B1) in the form

$$\sum_{m_1m_2m_3} c_{m_1}c_{m_2}c_{m_3} \int_{\boldsymbol{q}} \frac{1}{q^{2\nu_1}|\boldsymbol{k}_1-\boldsymbol{q}|^{2\nu_2}|\boldsymbol{k}_2+\boldsymbol{q}|^{2\nu_3}} \tag{B2}$$

for $2\nu_j = \alpha_j - \nu - j\eta_{m_i}$, where all the cosmology dependence (encoded in c_m) is now outside the integral. The remaining integral can be computed using path integral methods as

$$\int_{\boldsymbol{q}} \frac{1}{q^{2\nu_1}|\boldsymbol{k}_1-\boldsymbol{q}|^{2\nu_2}|\boldsymbol{k}_2+\boldsymbol{q}|^{2\nu_3}} \equiv k^{3-2(\nu_1+\nu_2+\nu_3)}\mathsf{J}(\nu_1,\nu_2,\nu_3;x,y) \tag{B3}$$

where $x^2 = k_3/k_1$, $y^2 = k_2/k_1$ and J (with complex arguments ν_i) can be expressed as a sum of hypergeometric functions and Gamma functions [99]. This reduces the computation of bispectrum templates to a set of matrix multiplications and function evaluations, as noted in § III. For B^I_{321} we find a similar form to (3.1), except with rank-two matrices, whilst B^{II}_{321} and B_{411} involve only a one-dimensional sum (and one set of c_{m_i} coefficients).

b. Limiting behavior

When computing spectra via FFTLog, it is important to verify whether the relevant loop integrals actually converge. This is achieved by taking the UV and IR limits of the integration kernels and assessing the dependence on the ν_i parameters appearing in (B2). As an example, we consider the contribution of three δ operators to B_{222} [involving three copies of $b_1F_2(\boldsymbol{k}-\boldsymbol{q},\boldsymbol{q})$]. This has the following limits in the equilateral configuration $k_1 \sim k_2 \sim k_3 \sim k$:

$$B^{\rm UV}_{222}(\boldsymbol{k}_1,\boldsymbol{k}_2,\boldsymbol{k}_3) \supset \frac{89}{2401}{b_1}^3k^6\int_{\boldsymbol{q}}\frac{P_L^3(q)}{q^6},$$
$$B^{\rm IR}_{222}(\boldsymbol{k}_1,\boldsymbol{k}_2,\boldsymbol{k}_3) \supset \frac{2}{21}{b_1}^3k^2P_L^2(k)\int_{\boldsymbol{q}}\frac{P_L(q)}{q^2}. \tag{B4}$$

For $P_L(q) \sim q^\nu$, the integral is UV convergent for $\nu < 1$ and IR convergent for $\nu > -1$. By choosing the bias in this range, FFTLog will give accurate values for the integrals. In contrast, if ν is chosen to be outside this range, we must add the relevant UV or IR limits by hand (taking care to include subleading divergences if necessary).

Considering all bias terms, the limits of B_{222} take the following schematic form for equilateral triangles:

$$B^{\rm UV}_{222} \sim \int_{\boldsymbol{q}} P_L^3(q)\left\{{b_2}^3 + \left(\frac{k}{q}\right)^2{b_2}^2f_1(b_1,\gamma_2) + \left(\frac{k}{q}\right)^4b_2f_2(b_1,\gamma_2) + \left(\frac{k}{q}\right)^6f_2(b_1,\gamma_2)\right\}$$
$$B^{\rm IR}_{222} \sim P_L^2(k)\int_{\boldsymbol{q}} P_L(q)\left\{\left(\frac{k}{q}\right)^2[{b_1}^3f_4 + {b_1}^2f_5(b_2,\gamma_2)] + [b_1f_6(b_2,\gamma_2) + f_7(b_2,\gamma_2)]\right\}, \tag{B5}$$

where $\{f_i\}$ are some polynomials, and we consider only the leading-order contribution for each bias parameter. Inserting $P_L(q) \sim q^\nu$ as before shows that a term containing K powers of b_2 is UV convergent for $\nu < 1–2K/3$, implying $\nu < -1$ for b_2^3, significantly tighter than the $\nu < 1$ limit for matter (i.e., b_1^3). However, the UV limit of b_2^3 is fully degenerate with the bispectrum shot noise (ϵ_0 in (2.13), and should be subtracted off in practice, as for the b_2^2 contribution to P_{22}. If we adopt $\nu > -1$, this term will not be captured by the FFTLog formalism, thus the subtraction becomes implicit. In this case, we require $\nu < -1/3$ to avoid the b_2^2 divergence [and the second-order b_2^3 divergence, both of which are degenerate with the ϵ_2 stochasticity in (2.13)]. In the IR, (B5) shows that the integral is convergent for $\nu > -1$ for terms involving two or more

powers of b_1, and $\nu > -3$ else. To satisfy all the conditions simultaneously, we may take $-1 < \nu < -1/3$, dropping the shot-noise piece.

For B^I_{321}, the limiting UV and IR form is given by

$$B^{I,\mathrm{UV}}_{321} \sim b_1 P_L(k) \int_{\boldsymbol{q}} P_L^2(q) \left\{ \frac{1}{2} X^2 + \left(\frac{k}{q}\right)^2 X f_1(\cdots) + \left(\frac{k}{q}\right)^4 f_2(\cdots) \right\},$$
$$B^{I,\mathrm{IR}}_{321} \sim b_1 P_L^2(k) \int_{\boldsymbol{q}} P_L(q) \left\{ \left(\frac{k}{q}\right)^2 [{b_1}^2 f_3(\cdots) + b_1 f_4(\cdots)] + f_6(\cdots) \right\}, \tag{B6}$$

where $X \in \{b_2, b_3, \gamma_2^\times\}$ and ellipses are taken to mean bias operators excluding X (in the UV) or b_1 (in the IR). Equation (B6) implies that UV divergences can be avoided if we take $\nu < (1-2K)/2$ when the term involves K powers of b_2, b_3, or $\gamma_2^\times$; these are all the composite operators appearing at third order. Furthermore, as in B_{222}, the UV limits of the terms involving two powers of b_2, b_3 and $\gamma_2^\times$ are proportional to shot noise (this time of the η_0 variety in (2.13),[10] and should be subtracted off in practice (or dropped implicitly by fixing $\nu > -3/2$). In the IR, divergences vanish for $\nu > -1$ for terms involving b_1^3 or b_1^2 and $\nu > -3$ else. Overall, we require a bias of $-1 < \nu < -1/2$ to satisfy all conditions, assuming subtraction of the η_0 shot-noise contributions.

For B^{II}_{321}, we require the UV and IR convergence properties of $\int_{\boldsymbol{q}} Z_3(\boldsymbol{k}, \boldsymbol{q}, -\boldsymbol{q}) P_L(q)$, which we label $\tilde{P}_{13}(k)$ by analogy with the galaxy power spectrum (2.9). This natively involves all bias operators in (2.2) up to third order; however, this set is reduced to just $\{\delta, \mathcal{G}_2(\Phi_v), \mathcal{G}_2(\varphi_2, \varphi_1)\}$ when the renormalization conditions are applied. These conditions demand

$$\lim_{k_1 \to 0} \langle X(\boldsymbol{k}) \delta_L(\boldsymbol{k}_1) \rangle'_{\mathrm{loop}} = 0 \tag{B7}$$

for renormalized operator X and linear density field $\delta_L(\boldsymbol{k})$, i.e., there can be no loop contributions which do not decay in the UV limit [107]. The contribution of all composite operators (e.g., δ^2) to $\tilde{P}_{13}$ is exactly that of a nondecaying loop diagram (since there is no suppression by the F_3 kernel), thus must vanish when the operators are properly renormalized. This leaves only $\mathcal{G}_3$, which evaluates to zero after averaging over the angular part of $\boldsymbol{q}$. Following these redefinitions (which do not affect B_{222} and B^I_{321}), we find the UV and IR limits:

$$\tilde{P}^{\mathrm{UV}}_{13} \sim \int_{\boldsymbol{q}} P_L(q) \left(\frac{k}{q}\right)^2 f_1(b_1, \gamma_2, \gamma_{21}),$$
$$\tilde{P}^{\mathrm{IR}}_{13} \sim \int_{\boldsymbol{q}} P_L(q) \left\{ \left(\frac{k}{q}\right)^2 b_1 f_2 + f_3(\gamma_2, \gamma_{21}) \right\}. \tag{B8}$$

UV divergences occur unless $\nu < -1$, and IR divergences occur unless $\nu > -1$ (for b_1) or $\nu > -3$ (else). As for P_{13} [99], there is no range of biases which satisfy all the conditions; in this case, we can choose $-1 < \nu < 1$ (satisfying the IR limits, and avoiding subleading UV divergences at $\nu > 1$), and correct the UV part by adding the relevant limit by hand, which takes the following explicit form in real space:

$$\tilde{P}^{\mathrm{UV}}_{13}(k) = -k^2 \left(\frac{61}{315} b_1 + \frac{64}{35} \gamma_2 - \frac{32}{15} \gamma_{21} \right) \int_0^\infty \frac{q^2 dq}{2\pi^2} \frac{P(q)}{q^2}, \tag{B9}$$

proportional to the velocity divergence σ_v^2.

Finally, we consider B_{411}. This contains the fourth-order bias operators, and involves Wick contractions of linear density fields within the same operator, permitting simplification via the renormalization condition:

$$\lim_{k_{1,2} \to 0} \langle X(\boldsymbol{k}) \delta_L(\boldsymbol{k}_1) \delta_L(\boldsymbol{k}_2) \rangle'_{\mathrm{loop}} = 0, \tag{B10}$$

which is proportional to the UV limit of B_{411}. The first effect of this is to remove contributions from any fourth-order composite local evolution operator (such as δ^4 or $\delta\mathcal{G}_3$); these operators were already dropped from the bias expansion in (2.2). Second, this will remove a number of UV divergences in the below. Before bias renormalization, the UV and IR limits of the remaining terms take the following form:

$$B^{\mathrm{UV}}_{411} \sim {b_1}^2 P_L^2(k) \int_{\boldsymbol{q}} P_L(q) \left\{ f_1(b_2, \gamma_2^\times, \gamma_{21}^\times) + \left(\frac{k}{q}\right)^2 f_2(\cdots) \right\}$$
$$B^{\mathrm{IR}}_{411} \sim {b_1}^2 P_L^2(k) \int_{\boldsymbol{q}} P_L(q) \left\{ \left(\frac{k}{q}\right)^2 f_3(b_1, b_2, \gamma_2) + f_4(\cdots) \right\}, \tag{B11}$$

where ellipses represent additional bias terms which impatience lead us to ignore. The first line is UV convergent for $\nu < -3$ (first term, involving composite operators) or $\nu < -1$ (second term, no composite operators). However, the first term possesses a UV limit that does not decay as an (negative) integer power of q^2, violating the renormalization condition (B10). The precise action of bias operator renormalization is to remove such terms (and only these, as far as this diagram is concerned). By evaluating the diagram with $\nu > -1$, such contributions will be avoided, i.e., the operators will be correctly renormalized.

[10] This occurs regardless of the triangle configuration, once permutations are taken into account.

In the IR, we find that divergences can be avoided by setting $\nu > -1$ (for terms involving the first and second order operators proportional to b_1, γ_2 or b_2), or $\nu > -3$ (for the remaining terms). As for $\tilde{P}_{13}$, there is no single bias that will simultaneously remove all the UV and IR divergences in B_{411}, even after bias renormalization. Fixing $-1<\nu<1$, we may compute the full expression by manually adding the appropriate UV limit to the FFTLog result. These limits can be computed straightforwardly from the kernels in *Mathematica* and are omitted from this publication to avoid unnecessary tedium.

2. Redshift space

In redshift-space the perturbation theory kernels depend not only on the lengths q, $|\boldsymbol{k}_1 - \boldsymbol{q}|$ and $|\boldsymbol{k}_2 + \boldsymbol{q}|$ but also the LOS angles $\mu_i \equiv \hat{\boldsymbol{k}}_i \cdot \hat{\boldsymbol{n}}$ and $\hat{\boldsymbol{q}} \cdot \hat{\boldsymbol{n}}$.[11] Although we are primarily interested only in the bispectrum monopole (i.e., that integrated over $\mu_{1,2}$, with a suitable Lebesque measure, as in (2.20)), the full dependence on μ_i is necessary for an accurate calculation of coordinate distortions (2.21), thus we cannot simply average over μ_i before computing the loop integrals; furthermore, this is difficult to perform analytically due to the presence of high powers of $\hat{\boldsymbol{q}} \cdot \hat{\boldsymbol{n}}$. After expanding the kernels as polynomials, we will find loop integrals of the following form:

$$\int_{\boldsymbol{q}} \frac{(\hat{\boldsymbol{q}} \cdot \hat{\boldsymbol{n}})^n}{q^{2\nu_1} |\boldsymbol{k}_1 - \boldsymbol{q}|^{2\nu_2} |\boldsymbol{k}_2 + \boldsymbol{q}|^{2\nu_3}} \tag{B12}$$

for $n \in \{0, 1, \ldots, 6\}$ [cf. (3.1)], with prefactors depending on μ_i, k_i, biases and $f(z)$. Below, we consider how to compute this utilizing the FFTLog procedure, generalizing the approach of [113] for the power spectrum.

First, we expand the $\hat{\boldsymbol{q}} \cdot \hat{\boldsymbol{n}}$ angles as Cartesian sums, i.e., $\sum_{i=1}^{3} \hat{q}_i \hat{n}^i$, and pull out the LOS vectors from the integral. The remaining function is a fully symmetric rank-n tensor, given by

$$\mathcal{F}^{i_1 \cdots i_n} \equiv \int_{\boldsymbol{q}} \frac{\hat{q}^{i_1} \cdots \hat{q}^{i_n}}{q^{2\nu_1} |\boldsymbol{k}_1 - \boldsymbol{q}|^{2\nu_2} |\boldsymbol{k}_2 + \boldsymbol{q}|^{2\nu_3}}. \tag{B13}$$

This has dependence only on $\boldsymbol{k}_1$ and $\boldsymbol{k}_2$; as such, its tensorial dependence can be written in terms of the components of $\boldsymbol{k}_1$, $\boldsymbol{k}_2$, and any isotropic tensors of relevance, i.e., the Kronecker delta.[12] Explicitly, this takes the following form:

$$\mathcal{F}^{i_1 \cdots i_n} = \sum_k A_k \mathcal{O}_k^{i_1 \cdots i_n}, \tag{B14}$$

where $\{\mathcal{O}_k\}$ is the set of all independent symmetric rank-n combinations of $\hat{k}_1^i$, $\hat{k}_2^i$, and $\delta_{\rm K}^{ij}$. As an example, the $n = 2$ operators are $\{\delta_{\rm K}^{ij}, \hat{k}_1^i \hat{k}_1^i, \hat{k}_1^i \hat{k}_2^j + \hat{k}_2^i \hat{k}_1^j, \hat{k}_2^i \hat{k}_2^j\}$. We then define an "overlap matrix," giving the correlation between basis elements:

$$\mathcal{I}_{kk'} = \mathcal{O}_k^{i_1 \cdots i_n} \mathcal{O}^{k'}_{i_1 \cdots i_n} \tag{B15}$$

(assuming Einstein summation conventions); this allows extraction of the A_k coefficients via $A_k = [\mathcal{I}]^{-1}_{kk'} \mathcal{O}^{k'}_{i_1 \cdots i_n} \mathcal{F}^{i_1 \cdots i_n}$, where the second term is just the contraction of (B14) with various powers of $\hat{\boldsymbol{k}}_1$ and $\hat{\boldsymbol{k}}_2$. Finally, we contract (B14) with n copies of $\hat{n}_i$ to yield

$$\begin{aligned} &\int_{\boldsymbol{q}} \frac{(\hat{\boldsymbol{q}} \cdot \hat{\boldsymbol{n}})^n}{q^{2\nu_1} |\boldsymbol{k}_1 - \boldsymbol{q}|^{2\nu_2} |\boldsymbol{k}_2 + \boldsymbol{q}|^{2\nu_3}} \\ &\quad = ([\mathcal{I}]^{-1}_{kk'} \mathcal{O}^{k'}_{i_1 \cdots i_n} \mathcal{F}^{i_1 \cdots i_n})(\mathcal{O}_k^{i_1 \cdots i_n} \hat{n}_{i_1} \cdots \hat{n}_{i_n}), \end{aligned} \tag{B16}$$

where the first set of parentheses contains a set of $\hat{\boldsymbol{k}}_{1,2} \cdot \hat{\boldsymbol{q}}$ coefficients inside the $\boldsymbol{q}$ integral, and the second contains powers of $\mu_{1,2}$. To make this explicit, we give the $n = 1$ case:

$$\begin{aligned} &\int_{\boldsymbol{q}} \frac{(\hat{\boldsymbol{q}} \cdot \hat{\boldsymbol{n}})}{q^{2\nu_1} |\boldsymbol{k}_1 - \boldsymbol{q}|^{2\nu_2} |\boldsymbol{k}_2 + \boldsymbol{q}|^{2\nu_3}} \\ &\quad = \frac{\mu_1 - \mu_2 \nu_{12}}{1 - \nu_{12}^2} \int_{\boldsymbol{q}} \frac{\hat{\boldsymbol{q}} \cdot \hat{\boldsymbol{k}}_1}{q^{2\nu_1} |\boldsymbol{k}_1 - \boldsymbol{q}|^{2\nu_2} |\boldsymbol{k}_2 + \boldsymbol{q}|^{2\nu_3}} \\ &\qquad + \frac{\mu_2 - \mu_1 \nu_{12}}{1 - \nu_{12}^2} \int_{\boldsymbol{q}} \frac{\hat{\boldsymbol{q}} \cdot \hat{\boldsymbol{k}}_2}{q^{2\nu_1} |\boldsymbol{k}_1 - \boldsymbol{q}|^{2\nu_2} |\boldsymbol{k}_2 + \boldsymbol{q}|^{2\nu_3}}, \end{aligned} \tag{B17}$$

writing $\nu_{12} \equiv \hat{\boldsymbol{k}}_1 \cdot \hat{\boldsymbol{k}}_2$. In this manner, the FFTLog integral can be performed for arbitrarily large n. We adopt this method to compute the bispectrum templates in redshift space, applying it as a simplification step before the loop integrals are computed as in Appendix B 1.

Notably, the above decomposition breaks down in the limit of $\hat{\boldsymbol{k}}_1 \cdot \hat{\boldsymbol{k}}_2 \to -1$, i.e., for $\boldsymbol{k}_1 \| \boldsymbol{k}_2$, whence there is only one angle in the problem. This corresponds to flattened triangles (with $k_1 = k_2 + k_3$ or $\sqrt{x} + \sqrt{y} = 1$), which contain the divergence $1 - \nu_{12}^2 \to 0$. Strictly speaking, this divergence is canceled by the numerators, once $\hat{\boldsymbol{k}}_1 = -\hat{\boldsymbol{k}}_2$ is identified; however, if one separately computes the loop integral coefficients proportional to powers of μ_1 and μ_2, numerical issues will arise. In this limit, we adopt a different angular decomposition, noting that (B13) can depend only on $\hat{\boldsymbol{k}}_1$ and the Kronecker delta. The basis tensors are much simpler in this case, for example, with $\{\delta_{\rm K}^{ij}, \hat{k}_1^i \hat{k}_1^j\}$ for $n = 2$, and facilitate computation in an analogous manner to the above. For $n = 1$, (B17) becomes

[11] In the isotropic approximation of infrared resummation (§ II) the angular dependence is purely polynomial.

[12] Note that the Levi-Cevita tensor, which is relevant for rank-three tensors and above, does not contribute to the expansion of (B13), since it is antisymmetric.

$$\int_{\boldsymbol{q}} \frac{(\hat{\boldsymbol{q}}\cdot\hat{\boldsymbol{n}})}{q^{2\nu_1}|\boldsymbol{k}_1-\boldsymbol{q}|^{2\nu_2}|\boldsymbol{k}_2+\boldsymbol{q}|^{2\nu_3}}\bigg|_{\rm flat} = \mu_1\int_{\boldsymbol{q}} \frac{\hat{\boldsymbol{q}}\cdot\hat{\boldsymbol{k}}_1}{q^{2\nu_1}|\boldsymbol{k}_1-\boldsymbol{q}|^{2\nu_2}|\boldsymbol{k}_2+\boldsymbol{q}|^{2\nu_3}}, \tag{B18}$$

which does not diverge. This divergence also illustrates the importance of expanding the bispectrum templates in the $\{\mu,\chi\}$ basis (with $\mu\equiv\mu_1$, $\chi\equiv\sqrt{1-\mu^2}\cos\phi$) rather than $\{\mu_1,\mu_2\}$ (cf. § III): the former is undefined for flattened triangles, whence $\mu_1=-\mu_2$, whilst the latter simply has dependence only on μ in this limit (noting that $\mu_2=\mu\nu_{12}-\sqrt{1-\nu_{12}^2}\chi\to-\mu$ as $\nu_{12}\to-1$).

3. Implementation

The above tricks allow us to efficiently compute the one-loop bispectrum in redshift space. A rough overview of the computation is the following:

(1) Expand the relevant (symmetrized) perturbation theory kernels as polynomials in q, $|\boldsymbol{k}_i\pm\boldsymbol{q}|$, μ_i and $\hat{\boldsymbol{q}}\cdot\hat{\boldsymbol{n}}$.
(2) Replace powers of $\hat{\boldsymbol{q}}\cdot\hat{\boldsymbol{n}}$ with (B16) and expand.
(3) Create lookup tables giving each $\{\nu_1,\nu_2,\nu_3\}$ triplet of FFTLog frequencies and the associated coefficient (depending on biases and μ_i).
(4) Switch from the native $\{\mu_1,\mu_2,\mu_3\}$ basis to the (divergence-free) $\{\mu,\chi\}$ angular basis.
(5) Compute the bispectrum templates for each of the 47 combinations of $\mu^i\chi^j$ and the relevant combinations of bias parameters using the FFTLog algorithm. This is performed for a grid of values of k_1,x,y, with flattened templates (obeying $\sqrt{x}+\sqrt{y}=1$) computed separately, using the alternate angular decomposition given in Appendix B 2, and involving only seven nontrivial powers of μ.
(6) Create a three-dimensional linear interpolator for each template using the precomputed bispectrum shapes (combining full and flattened configurations).
(7) Apply binning and angular integration using (3.4), including the Alcock-Paczynski parameters if necessary.
(8) Compute the full bispectrum as a sum over templates, weighted by the bias configurations and any necessary discreteness weights.

Notably, only steps (5) and beyond depend on the power spectrum template, and thus the cosmological survey in question. We note one further subtlety: computing the bispectrum templates near (but not at) the flattened limit of $\sqrt{x}+\sqrt{y}=1$ can lead to numerical issues due to large values of $1/(1-\nu_{12}^2)$, which appear in the angular decompositions of $(\hat{\boldsymbol{q}}\cdot\hat{\boldsymbol{n}})$ raised to the nth power [cf. (B17)]. To counter this, when the templates are being computed and the condition $\sqrt{x}+\sqrt{y}<1.1$ is met, we replace the FFTLog prefactor by its Taylor series in $(1+\nu_{12})$, artificially removing the divergent terms (which are present only due to numerical inaccuracies). *Mathematica* and PYTHON code implementing all of the above steps is publicly available at GitHub.com/OliverPhilcox/OneLoopBispectrum.

Following initial testing of the FFTLog routines against explicit numerical integration for a small number of bins, we use the following choices of FFTLog bias: $\nu=-0.6$ for B_{222} and B_{321}^{II}, $\nu=-0.3$ for the matter terms in B_{321}^{I} (i.e., those involving only b_1 and f) and B_{411}, and $\nu=-0.8$ for the remaining terms in B_{321}^{I}. We additionally use 64 FFTLog frequencies for B_{222}, 96 frequencies for B_{321}^{I}, and 128 frequencies for B_{321}^{II} and B_{411}, which reduces computational costs, whilst keeping good resolution on the terms with enhanced oscillatory behavior. Additionally, we manually add the UV limits of B_{321}^{II} and B_{411} (as in Appendix B 1), and choose the k range for the FFTLog decomposition to lie in $[10^{-5},10]\,h\,\mathrm{Mpc}^{-1}$, computing all shapes on an interpolation grid of 64 k_1 values logarithmically spaced in $[10^{-3},0.5]\,h\,\mathrm{Mpc}^{-1}$, and 41 equally spaced values of each of $\sqrt{x}$ and $\sqrt{y}$, subject to the triangle conditions. This is sufficient to ensure that the spectra are subpercent accurate in the regime of interest; the results are largely unchanged if the number of FFTLog frequencies is reduced by a factor of 2. The computation requires $\sim10^4$ CPU hours to compute all templates (entirely performed within *Mathematica*), with the majority of time devoted to B_{222}, and could certainly be optimized further. Calculations have been compared against explicit numerical integration of the (unsimplified) bispectrum kernels, and we find excellent subpercent agreement in all cases.

APPENDIX C: COUNTERTERMS FROM REDSHIFT-SPACE DISTORTIONS

The RSD mapping to $\mathcal{O}(\delta_1^4)$ can be obtained by expanding (2.7) to fourth order:

$$\delta_{\mathbf{k}}^{(s)} = \delta_{\mathbf{k}} - ik_z[(1+\delta_g)u_z]_{\mathbf{k}} + \frac{i^2}{2}k_z^2[(1+\delta_g)u_z^2]_{\mathbf{k}} - \frac{i^3}{3!}k_z^3[(1+\delta_g)u_z^3]_{\mathbf{k}} + \frac{i^4}{4!}k_z^4[v_z^4(1+\delta_g)]_{\mathbf{k}}, \tag{C1}$$

where $A_z\equiv\boldsymbol{A}\cdot\hat{n}\equiv A\mu_A$. To facilitate renormalization, we must smooth this expansion with a low-pass filter of some size $R=\Lambda^{-1}$. Products of fields at the same point (contact terms) are sensitive to short-scaled modes and hence must to be smoothed and renormalized. We denote these operations by square brackets, $[\ldots]_R$. Galilean symmetry implies the following schematic structure of the renormalized correlators (see [141–143] for the first order results),

$$
\begin{aligned}
[u^i(1+\delta_g)]_R &= (1+\delta_{g\ell})u^i_\ell + \mathcal{O}^i_u,\\
[u^i v^j(1+\delta_g)]_R &= (1+\delta_{g\ell})u^i_\ell u^j_\ell + u^i_\ell \mathcal{O}^{(1)j}_{u^2} + u^j_\ell \mathcal{O}^{(1)i}_{u^2} + \mathcal{O}^{(2)ij}_{u^2},\\
[u^i u^j u^k(1+\delta_g)]_R &= (1+\delta_{g\ell})u^i_\ell u^j_\ell u^k_\ell + 3u^2_\ell \mathcal{O}^{(1)ijk}_{u^3} + 3u_\ell \mathcal{O}^{(2)ijk}_{u^3} + \mathcal{O}^{(3)ijk}_{u^3},\\
[u^i u^j u^k u^l(1+\delta_g)]_R &= (1+\delta_{g\ell})u^i_\ell u^j_\ell u^k_\ell u^l_\ell + 4u^3_\ell \mathcal{O}^{(1)ijkl}_{u^4} + 6u^2_\ell \mathcal{O}^{(2)ijkl}_{u^4} + 4u_\ell \mathcal{O}^{(3)ijkl}_{u^4} + \mathcal{O}^{(4)ijkl}_{u^4},
\end{aligned}
\tag{C2}
$$

where u^i_ℓ, δ_ℓ are the smoothed long-wavelength velocity and density fields (for clarity, we will drop the subscript ℓ in the below). To preserve Galilean symmetry, the operators $\mathcal{O}$ should not depend on the smoothed velocity field.

Note that the velocity field scales like $k^{-1}\delta_{\mathbf{k}}$ at the linear order, i.e.,

$$
u_i = -\frac{\partial_i}{\Delta}\theta, \tag{C3}
$$

for Laplacian Δ. Thus, in order to obtain the redshift-space bispectrum counterterms scaling like $k^2\delta^2$, we need to retain four types of correction: (1) $\mathcal{O}(k^1\delta^2)$ arising from $[u^i(1+\delta_g)]_R$, (2) $\mathcal{O}(k^0\delta^2)$ coming from $[u^i u^j(1+\delta_g)]_R$, (3) $\mathcal{O}(k^{-1}\delta^2)$ coming from $[u^i u^j u^k(1+\delta_g)]_R$, and (4) $\mathcal{O}(k^{-2}\delta^2)$ coming from $[u^i u^j u^k u^l(1+\delta_g)]_R$.

We now discuss each type of composite operator. The renormalized operator $[u^i(1+\delta_g)]_R$ with counterterms $\mathcal{O}(k\delta^2)$ is given by

$$
\begin{aligned}
[u^i(1+\delta_g)]_R = u^i(1+\delta) &+ \tilde{e}_1\partial_i\delta + \tilde{e}_2\partial_i(s_{kl}s^{kl})\\
&+ \tilde{e}_3\partial_i\delta^2 + \tilde{e}_4 s_{kl}\partial_i s^{kl} + \tilde{e}_5\delta\partial_i\delta,
\end{aligned}
\tag{C4}
$$

where δ is the matter density field and we have introduced the tidal tensor $s_{ij} = [\partial_i\partial_j\Phi - \delta_{ij}(\Delta\Phi/3)]/(\frac{3}{2}\mathcal{H}^2)$. The renormalized operator $[u^i u^j(1+\delta_g)]_R$ with counterterms $\mathcal{O}(k^0\delta^2)$ is given by

$$
\begin{aligned}
[u^i u^j(1+\delta_g)]_R = u^i u^j(1+\delta) &+ \tilde{c}_1\delta_{ij}\delta + \tilde{c}_2 s_{ij}\\
&+ c_3\delta^2\delta_{ij} + \tilde{c}_4 s_{il}s_{lj},
\end{aligned}
\tag{C5}
$$

The renormalized operator $[u^i u^j u^k(1+\delta_g)]_R$ with counterterms $\mathcal{O}(k^{-1}\delta^2)$ is given by

$$
\begin{aligned}
[u^i u^j u^k(1+\delta_g)]_R = u^i u^j u^k(1+\delta) &+ \tilde{b}_1 u_{(i}\delta_{jk)}\\
&+ \tilde{b}_2 u_{(i}s_{jk)} + \tilde{b}_3\delta u_{(i}\delta_{jk)},
\end{aligned}
\tag{C6}
$$

where (...) denotes symmetrization over indices. Finally, the renormalized operator $[u^i u^j u^k u^l(1+\delta_g)]_R$ with counterterms $\mathcal{O}(k^{-2}\delta^2)$ is given by

$$
[u^i u^j u^k u^m(1+\delta)]_R = u^i u^j u^k u^m(1+\delta_g) + \tilde{d}_1 u_{(i}u_j\delta_{kl)}. \tag{C7}
$$

In combination, once certain redundant operators are removed, we find the following redshift-space bispectrum counterterm kernel,

$$
\begin{aligned}
Z_2^{\rm ctr}(\mathbf{k}_1,\mathbf{k}_2) = \Bigg(& C_1\mu^2 k_3^2 F_2(\mathbf{k}_1,\mathbf{k}_2) + C_2 k_{3z}^2\left(\mu_3^2 - \frac{1}{3}\right)F_2(\mathbf{k}_1,\mathbf{k}_2) + C_3 k_{3z}^2 + C_4 k_{3z}^2\left(\frac{(\mathbf{k}_1\cdot\mathbf{k}_2)\mu_1\mu_2}{k_1k_2} - \frac{\mu_1^2+\mu_2^2}{3} + \frac{1}{9}\right)\\
& + C_5 f k_{3z}^2\mu_3^2 G_2(\mathbf{k}_1,\mathbf{k}_2) + C_6 f k_{3z}^3\left[\frac{\mu_1}{k_1}\left(\mu_2 - \frac{1}{3}\right) + \frac{\mu_2}{k_2}\left(\mu_1 - \frac{1}{3}\right)\right] + C_7 f k_z^3\left[\frac{\mu_1}{k_1} + \frac{\mu_2}{k_2}\right] + C_8 f^2 k_{3z}^4\frac{\mu_1}{k_1}\frac{\mu_2}{k_2}\\
& + C_9 k_{3z}^2\left(\frac{(\mathbf{k}_1\cdot\mathbf{k}_2)^2}{k_1^2k_2^2} - \frac{1}{3}\right)\Bigg)\frac{1}{k_{\rm NL}^2},
\end{aligned}
\tag{C8}
$$

involving nine Wilson coefficients, marked in color. The overall bispectrum counterterm is given by

$$
\begin{aligned}
B_{\rm ctr}(\mathbf{k}_1,\mathbf{k}_2,\mathbf{k}_3) = &\, 2Z_1(\mathbf{k}_1)Z_1(\mathbf{k}_2)(F_2^{\rm ctr} + Z_2^{\rm ctr})(\mathbf{k}_1,\mathbf{k}_2)\\
&\times P_{11}(k_1)P_{11}(k_2) + \text{cyclic perms.},
\end{aligned}
\tag{C9}
$$

where $F_2^{\rm ctr}(\mathbf{k}_1,\mathbf{k}_2)$ is the real space, μ-independent kernel. In principle, some of the redshift-space counterterms are the same as coefficients in front of the μ-dependent k^2P_{11} redshift-space counterterms in redshift space, and thus should be constrained by the power spectrum data. Indeed, at leading order we have [143]

$$
\delta_z^{\rm CTR,LO}(\mathbf{k}) = \mathcal{C}_0 k^2\delta + \mathcal{C}_1\mu^2k^2\delta + \mathcal{C}_2\mu^4k^2\delta, \tag{C10}
$$

where

$$\mathcal{C}_1 = C_1 - \frac{C_2}{3}, \qquad \mathcal{C}_2 = C_2 + C_5 f. \tag{C11}$$

The relationship between our power spectrum counterterm coefficients ($\propto k^2 P_L$) and $\mathcal{C}_n$ is given by

$$\begin{aligned} c_0 &= b_1\left(\mathcal{C}_0 + \frac{\mathcal{C}_1}{3} + \frac{\mathcal{C}_2}{5}\right) + \frac{\mathcal{C}_0 f}{3} + \frac{\mathcal{C}_1 f}{5} + \frac{\mathcal{C}_2 f}{7}, \\ c_2 &= \frac{1}{7f}(7b_1\mathcal{C}_1 + 6b_1\mathcal{C}_2 + 7\mathcal{C}_0 f + 6\mathcal{C}_1 f + 5\mathcal{C}_2 f), \\ c_4 &= \frac{1}{11f^2}(11b_1\mathcal{C}_2 + 11\mathcal{C}_1 f + 15\mathcal{C}_2 f). \end{aligned} \tag{C12}$$

APPENDIX D: STOCHASTIC TERMS

In this section we discuss stochastic contributions to the one-loop bispectrum.

1. Real space

The stochastic contributions to the galaxy density field in real space are given in terms of ϵ by (some operators are presented in [143])

$$\begin{aligned} \delta_\epsilon = {} & d_1\epsilon + d_2\epsilon\delta + \bar{d}_1\left(\frac{k}{k_{\rm NL}}\right)^2\epsilon + d_2\left(\frac{k}{k_{\rm NL}}\right)^2[\epsilon\delta]_{\mathbf{k}} \\ & + d_3[\partial^i\epsilon\partial_i\delta]_{\mathbf{k}} + d_4[\epsilon\Delta\delta]_{\mathbf{k}} + d_5[\Delta\epsilon\delta]_{\mathbf{k}}. \end{aligned} \tag{D1}$$

Note that $\langle\epsilon\delta\rangle = 0$ by definition. There are two nontrivial possibilities to contract operators in δ_ϵ to obtain the tree-level bispectrum contributions (with free coefficients shown in color):

$$\begin{aligned} \mathcal{O}(P\bar{n}^{-1}):\ \langle b_1\delta_{\mathbf{k}_1} d_2[\epsilon\delta]_{\mathbf{k}_2}\epsilon_{\mathbf{k}_3}\rangle' &= 2d_2\frac{b_1 P(k_1) + \text{cyc.}}{\bar{n}}, \\ \mathcal{O}(\bar{n}^{-2}):\ \langle\epsilon^3\rangle' &= \frac{{d_1}^3 A_{\rm shot}}{\bar{n}^2}, \end{aligned} \tag{D2}$$

where primes denote that we drop the Dirac delta function. These match the operators present in the tree-level bispectrum model [80]. At the one-loop order we find three distinct contractions:

$$\begin{aligned} &\mathcal{O}(k^2 P\bar{n}^{-1}):\ \langle b_1\delta_{\mathbf{k}_1}\bar{d}_2 k_2^2[\epsilon\delta]_{\mathbf{k}_2}\epsilon_{\mathbf{k}_3}\rangle' \\ &\quad = b_1\bar{d}_2\frac{(k_2^2 + k_3^2)P(k_1) + \text{cyc.}}{\bar{n}}, \\ &\mathcal{O}(k^2 P\bar{n}^{-1}):\ \langle b_{\nabla^2\delta}k_1^2\delta_{\mathbf{k}_1} d_2[\epsilon\delta]_{\mathbf{k}_2}\epsilon_{\mathbf{k}_3}\rangle' \\ &\quad = b_{\nabla^2\delta}d_2\frac{k_1^2 P(k_1) + \text{cyc.}}{\bar{n}}, \\ &\mathcal{O}(k^2\bar{n}^{-2}):\ \langle\bar{d}_1 k_1^2\epsilon_{\mathbf{k}_1}\epsilon_{\mathbf{k}_2}\epsilon_{\mathbf{k}_3}\rangle' = \bar{d}_1 A_{\rm shot}\frac{k_1^2 + \text{cyc.}}{\bar{n}^2}. \end{aligned} \tag{D3}$$

These reproduce the stochastic bispectrum contribution derived in [79].

2. Redshift space

In redshift space, the density field involves the following terms at tree level:

$$\begin{aligned} \delta^{(z)}(\mathbf{k}) = {} & Z_1(\mathbf{k})\delta^{(1)}(\mathbf{k}) + [Z_2(\delta^{(1)})^2]_{\mathbf{k}} + d_1\epsilon_{\mathbf{k}} \\ & + d_2 b_1[\delta^{(1)}\epsilon]_{\mathbf{k}} - ifk_z d_1\left[\epsilon\frac{\hat{\hat{z}}_i\partial_i}{\Delta}\theta^{(1)}\right]_{\mathbf{k}}, \end{aligned} \tag{D4}$$

whilst at next-to-leading order (i.e., one-loop), we have the additional stochastic contributions

$$\delta^{(\mu^2k^2)}_{\rm stoch}(\mathbf{k}) = (d_1 f\mu^2 k^2\epsilon + k_z z^i(\epsilon^i + k^i\epsilon) + k_z^2 z_i z_j\epsilon^{ij})(1+\delta_g). \tag{D5}$$

At leading order we have the LOS-dependent $P\bar{n}^{-1}$ term derived in [80]. To obtain the one-loop expression, we must perform a renormalization of the contact operators involving the stochastic fields, as in Appendix C. The contact operator renormalization $\mathcal{O}(\epsilon, \epsilon\delta)$ at the leading order in derivatives, gives the following terms, schematically:

$$\begin{aligned} [u_i(1+\delta_g)]_R &\supset u_i^{(1)}\epsilon + (\epsilon_i + k_i\epsilon)(1+\delta_g) + \epsilon\partial_i\delta + \partial_i(\epsilon\delta), \\ [u_i u_j(1+\delta_g)]_R &\supset (\delta_{ij}\epsilon + \epsilon_{ij})(1+\delta) + u_i^{(1)}\epsilon_j \\ &\quad + u_i^{(1)}k_j\epsilon + s_{ij}\epsilon, \\ [u_i u_j u_k(1+\delta_g)]_R &\supset u_i^{(1)}\delta_{jk}\epsilon + u_i^{(1)}\epsilon_{jk}. \end{aligned} \tag{D6}$$

These operators generate the following LOS-dependent correction to the stochastic component of the galaxy density field:

$$\begin{aligned} \delta_{\rm stoch} \supset {} & k_z u_z^{(1)}\epsilon + k_z[(\epsilon_i z^i + \partial_z\epsilon)(1+\delta_g)] \\ & + k_z^2(\epsilon + \epsilon_{zz})(1+\delta_g) + k_z^2 u_z^{(1)}\epsilon_z \\ & + k_z^2 u_z^{(1)}[\partial_z\epsilon] + k_z^3(u_z^{(1)}\epsilon + u_z^{(1)}\epsilon_{zz}) \\ & + k_z(\epsilon[\partial_z\delta]) + k_z[\partial_z(\epsilon\delta)] + k_z^2[\epsilon s_{zz}]. \end{aligned} \tag{D7}$$

Focussing on the $k^2P(k)/\bar{n}$ corrections to the bispectrum that are generated by this density field (D7), we find three possibilities:

(1) Insertion of the redshift-space counterterms $k^2\delta$ and the real-space operator $d_2\delta\epsilon$, i.e., $\langle k^2\delta[\epsilon\delta]\epsilon\rangle$:

$$\begin{aligned} &\langle k_1^2\mu_1^{2\alpha}\delta_{\mathbf{k}_1} d_2[\epsilon\delta]_{\mathbf{k}_2}\epsilon_{\mathbf{k}_3}\rangle' = d_2\frac{k_1^2\mu_1^{2\alpha}P_L(k_1) + \text{cyc.}}{\bar{n}}, \\ &\left\langle k_1^2\mu_1^{2\alpha}\delta_{\mathbf{k}_1} ifk_{2z}d_1\left[\epsilon\frac{\hat{\hat{z}}_i\partial_i}{\Delta}\theta^{(1)}\right]_{\mathbf{k}_2}\epsilon_{\mathbf{k}_3}\right\rangle' \\ &\quad = -fd_1\frac{k_1^2\mu_1^{2\alpha+2}P_L(k_1) + \text{cyc.}}{\bar{n}}, \end{aligned} \tag{D8}$$

where $\alpha = 0, 1, 2$.

(2) Insertion of the redshift-space stochastic counterterm $\sim k^2\epsilon$ and the real-space operator $d_2\delta\epsilon$, i.e.,

$$\langle Z_1(\mathbf{k}_1)\delta_{\mathbf{k}_1} d_2[\epsilon\delta]_{\mathbf{k}_2} k_{3z}^2\epsilon_{\mathbf{k}_3}\rangle' = d_2\frac{Z_1(\mathbf{k}_1)P_L(k_1)(k_{2z}^2+k_{3z}^2)+\text{cyc.}}{\bar{n}}. \tag{D9}$$

(3) Insertion of the new redshift-dependent stochastic correction $k_z^2[\delta\epsilon]$, i.e.,

$$\begin{aligned}
&\langle Z_1(\mathbf{k}_1)\delta_{\mathbf{k}_1} k_{2z}^2[\epsilon\delta]_{\mathbf{k}_2}\epsilon_{\mathbf{k}_3}\rangle' = \frac{Z_1(\mathbf{k}_1)P_L(k_1)(k_{2z}^2+k_{3z}^2)+\text{cyc.}}{\bar{n}},\\
&\langle Z_1(\mathbf{k}_1)\delta_{\mathbf{k}_1} k_{2z}[\partial_z\epsilon\delta]_{\mathbf{k}_2}\epsilon_{\mathbf{k}_3}\rangle' = \frac{Z_1(\mathbf{k}_1)P_L(k_1)k_{2z}k_{3z}+\text{cyc.}}{\bar{n}},\\
&\left\langle Z_1(\mathbf{k}_1)\delta_{\mathbf{k}_1} k_{2z}^2\left[\partial_z\epsilon\frac{\partial_z\theta}{\Delta}\right]_{\mathbf{k}_2}\epsilon_{\mathbf{k}_3}\right\rangle' = -\frac{Z_1(\mathbf{k}_1)P_L(k_1)\mu_1^2k_{2z}k_{3z}+\text{cyc.}}{\bar{n}},\\
&\left\langle Z_1(\mathbf{k}_1)\delta_{\mathbf{k}_1} k_{2z}^3\left[\epsilon\frac{\partial_z\theta}{\Delta}\right]_{\mathbf{k}_2}\epsilon_{\mathbf{k}_3}\right\rangle' = \left(Z_1(\mathbf{k}_1)P_L(k_1)\frac{k_{1z}}{k_1^2}(k_{2z}^3+k_{3z}^3)+\text{cyc.}\right)\frac{1}{\bar{n}},\\
&\langle Z_1(\mathbf{k}_1)\delta_{\mathbf{k}_1} k_{2z}[\epsilon\partial_z\delta]_{\mathbf{k}_2}\epsilon_{\mathbf{k}_3}\rangle' = -\frac{Z_1(\mathbf{k}_1)P_L(k_1)k_{1z}^2+\text{cyc.}}{\bar{n}},\\
&\left\langle Z_1(\mathbf{k}_1)\delta_{\mathbf{k}_1} k_{2z}^2\left[\epsilon\left(\frac{\partial_z^2}{\Delta}-\frac{1}{3}\right)\delta\right]_{\mathbf{k}_2}\epsilon_{\mathbf{k}_3}\right\rangle' = \left(Z_1(\mathbf{k}_1)P_L(k_1)\left\{\mu_1^2-\frac{1}{3}\right\}(k_{2z}^2+k_{3z}^2)+\text{cyc.}\right)\frac{1}{\bar{n}},
\end{aligned} \tag{D10}$$

Many of these terms happen to be linearly dependent once we apply the bispectrum triangle condition. All in all, the μ-dependent part of the stochastic bispectrum at order $k^2P\bar{n}^{-1}$ is given by

$$\begin{aligned}
B_{\text{stoch}}^{(k^2P\bar{n}^{-1})}(\mathbf{k}_1,\mathbf{k}_2,\mathbf{k}_3) &= \Bigg[\sum_{n=1,2,3,4} S_n k_1^2\mu_1^{2(n-1)} + S_5Z_1(\mathbf{k}_1)(\mu_2^2k_2^2+\mu_3^2k_3^2)\\
&\quad + S_6Z_1(\mathbf{k}_1)\mu_1^2(\mu_2^2k_2^2+\mu_3^2k_3^2) + S_7Z_1(\mathbf{k}_1)\frac{k_{1z}}{k_1^2}(k_{2z}^3+k_{3z}^3)\Bigg]\\
&\quad\times\frac{P_L(k_1)}{k_{\text{NL}}^2\bar{n}}+\text{cyc.},
\end{aligned} \tag{D11}$$

which involves additional nuisance coefficients shown in color.

In addition, there are purely stochastic terms that generate the bispectrum of the order $k^2\bar{n}^{-2}$. These arise from the following combinations:

$$\langle\epsilon_{\mathbf{k}_1}\epsilon_{\mathbf{k}_2}k_{3z}^2\epsilon_{\mathbf{k}_3}\rangle' = \frac{k_{3z}^2+\text{cyc.}}{\bar{n}^2}, \tag{D12}$$

giving the bispectrum contribution

$$B_{\text{stoch}}^{(k^2\bar{n}^{-2})}(\mathbf{k}_1,\mathbf{k}_2,\mathbf{k}_3) = A_{\text{shot},2}\frac{k_{3z}^2+k_{1z}^2+k_{2z}^2}{\bar{n}^2}. \tag{D13}$$

After performing angular integration (in the absence of coordinate-distortion effects), this term takes the same form as the real-space term $\sim k^2\bar{n}^{-2}$. Thus, it does not produce a new contribution to the bispectrum monopole, though it is important if higher-order multipoles are also considered.

APPENDIX E: PRIOR VOLUME EFFECTS

In this section we study the prior volume effects present in our posteriors when the one-loop bispectrum likelihood is analyzed with small data cuts, such as $k_{\text{max}}^B = 0.12\,h\,\text{Mpc}^{-1}$. At face value, the posterior distributions from this analysis are several σ away from the true values. However, here we show that as much as half of this shift can be explained by prior volume (marginalization projection) effects. Indeed, such effects are expected to be present when the data volume is not sufficient to tightly constrain model parameters, which is the case for analyses with low k_{max}^B.

We performed the following test: rerunning our full analysis on the mock data generated by our fitting pipeline for the best-fit cosmology at $k_{\text{max}}^B = 0.15\,h\,\text{Mpc}^{-1}$. This mock data is simply a theory curve without any statistical scatter. In the absence of prior volume effects our pipeline must exactly recover the input parameters. However, when we fit this mock bispectrum data at $k_{\text{max}}^B = 0.12\,h\,\text{Mpc}^{-1}$, we find that the mean values recovered from our pipeline are shifted relative to the input values at the $(1\text{–}1.5)\sigma$ level, as shown in Fig. 5. This is evidence of prior volume effects. Furthermore, the shifts are in the directions of the apparent biases observed in the actual data (§VI). Thus, if we subtract these shifts from the actual posteriors at $k_{\text{max}}^B = 0.12$, the mean posterior values would match the true input parameter values at least within the 99% C.L. Finally, we note that the parameters b_2, $b_{\mathcal{G}_2}$, and b_{Γ_3} are highly correlated; this means that a shift in one would induce a shift in both.

As an additional check, we repeat our mock analysis for $k_{\text{max}}^B = 0.15\,h\,\text{Mpc}^{-1}$. Overall, we find much improved agreement between the mock and actual analyses, see Fig. 6. The posteriors for σ_8 and b_{Γ_3} are still shifted with respect to the ground truth by $\lesssim 1\sigma$ (which is smaller than 1.5σ shifts in the $k_{\text{max}}^B = 0.12\,h\,\text{Mpc}^{-1}$ case), but all other parameters are recovered without noticeable bias.

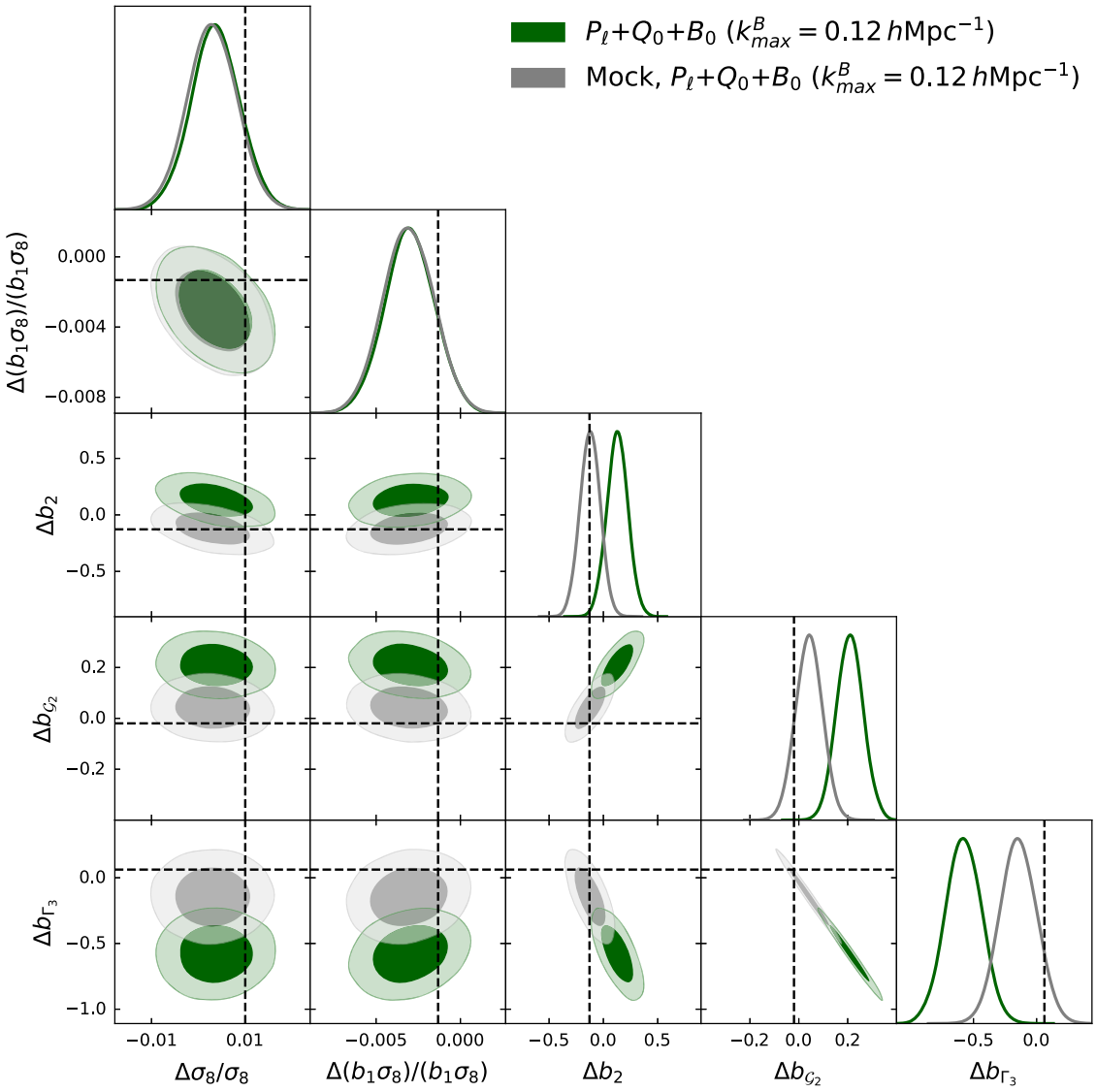

FIG. 5. Posterior distributions of the clustering amplitude and low-order nuisance parameters from MCMC analyses of the power spectrum and bispectrum likelihoods from the redshift-space analysis at $k^B_{\rm max} = 0.12\,h\,{\rm Mpc}^{-1}$ for the PT Challenge simulation data (in green) and for the mock bispectrum data vector (in gray) computed with our pipeline for the bestfit cosmology at $k^B_{\rm max} = 0.15\,h\,{\rm Mpc}^{-1}$. Dashed lines show the input values for the mock data vector, whose discrepancies with the gray posteriors indicate clear evidence for prior volume effects.

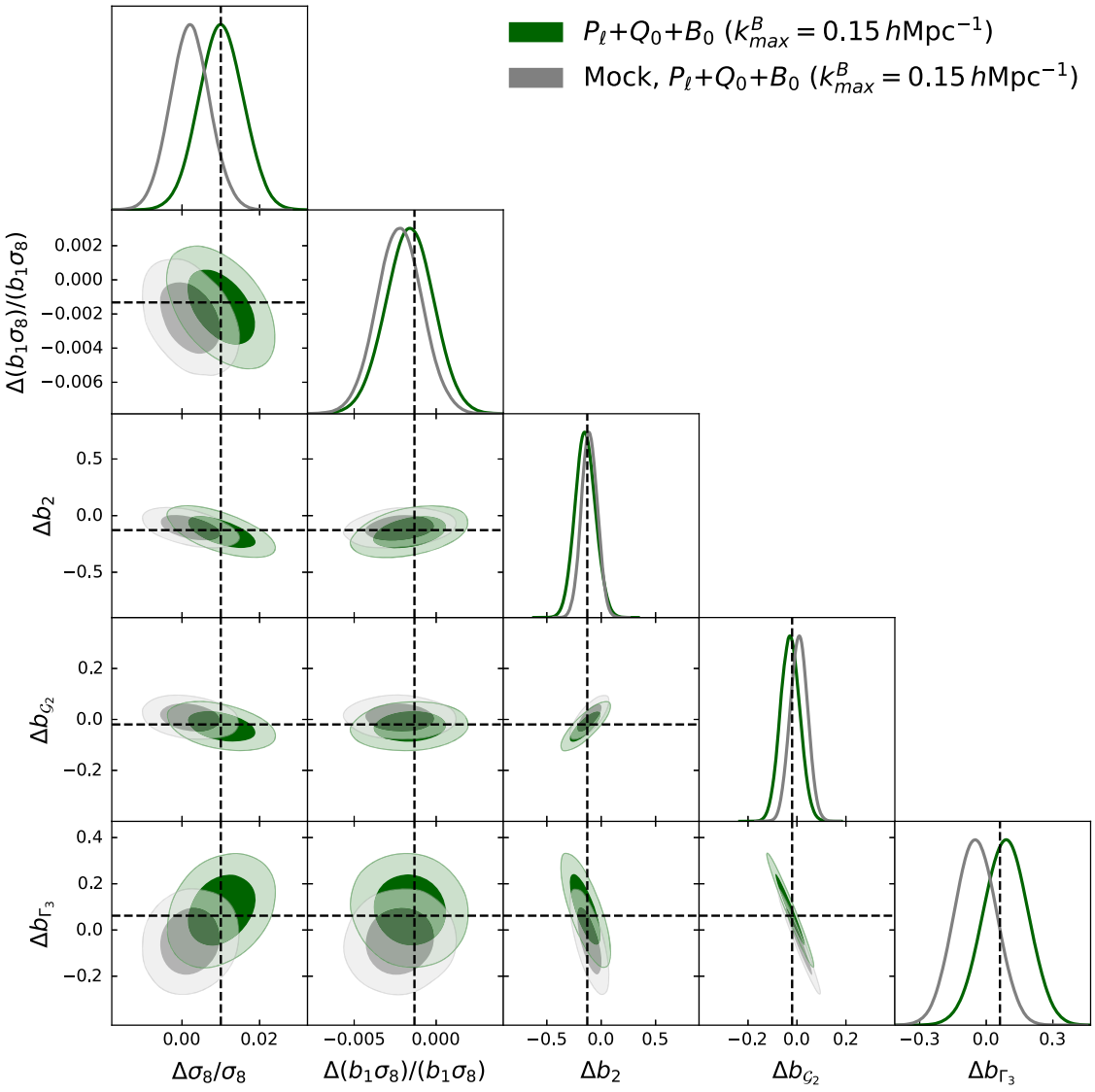

FIG. 6. As Fig. 5, but for $k^B_{\rm max}=0.15\,h\,{\rm Mpc}^{-1}$.

[1] J. N. Grieb *et al.* (BOSS Collaboration), The clustering of galaxies in the completed SDSS-III Baryon Oscillation Spectroscopic Survey: Cosmological implications of the Fourier space wedges of the final sample, Mon. Not. R. Astron. Soc. **467**, 2085 (2017).

[2] S. Alam *et al.* (BOSS Collaboration), The clustering of galaxies in the completed SDSS-III baryon oscillation spectroscopic survey: Cosmological analysis of the DR12 galaxy sample, Mon. Not. R. Astron. Soc. **470**, 2617 (2017).

[3] S. Satpathy *et al.* (BOSS Collaboration), The clustering of galaxies in the completed SDSS-III baryon oscillation spectroscopic survey: On the measurement of growth rate using galaxy correlation functions, Mon. Not. R. Astron. Soc. **469**, 1369 (2017).

[4] F. Beutler *et al.* (BOSS Collaboration), The clustering of galaxies in the completed SDSS-III baryon oscillation spectroscopic survey: Baryon acoustic oscillations in the Fourier space, Mon. Not. R. Astron. Soc. **464**, 3409 (2017).

[5] F. Beutler *et al.* (BOSS Collaboration), The clustering of galaxies in the completed SDSS-III baryon oscillation spectroscopic survey: Anisotropic galaxy clustering in fourier-space, Mon. Not. R. Astron. Soc. **466**, 2242 (2017).

[6] A. de Mattia *et al.*, The completed SDSS-IV extended baryon oscillation spectroscopic survey: Measurement of the BAO and growth rate of structure of the emission line galaxy sample from the anisotropic power spectrum between redshift 0.6 and 1.1, Mon. Not. R. Astron. Soc. **501**, 5616 (2021).

[7] S. Alam *et al.* (BOSS Collaboration), The clustering of galaxies in the completed SDSS-III baryon oscillation spectroscopic survey: Cosmological analysis of the DR12 galaxy sample, Mon. Not. R. Astron. Soc. **470**, 2617 (2017).

[8] S. Alam *et al.* (eBOSS Collaboration), Completed SDSS-IV extended baryon oscillation spectroscopic survey: Cosmological implications from two decades of spectroscopic surveys at the apache point observatory, Phys. Rev. D **103**, 083533 (2021).

[9] W. J. Percival *et al.*, The shape of the SDSS DR5 galaxy power spectrum, Astrophys. J. **657**, 645 (2007).

[10] M. M. Ivanov, M. Simonović, and M. Zaldarriaga, Cosmological parameters from the BOSS galaxy power spectrum, J. Cosmol. Astropart. Phys. 05 (2020) 042.

[11] M. M. Ivanov, M. Simonović, and M. Zaldarriaga, Cosmological parameters and neutrino masses from the final planck and full-shape BOSS data, Phys. Rev. D **101**, 083504 (2020).

[12] M. M. Ivanov, Cosmological constraints from the power spectrum of eBOSS emission line galaxies, Phys. Rev. D **104**, 103514 (2021).

[13] M. M. Ivanov, E. McDonough, J. C. Hill, M. Simonović, M. W. Toomey, S. Alexander, and M. Zaldarriaga, Constraining early dark energy with large-scale structure, Phys. Rev. D **102**, 103502 (2020).

[14] O. H. E. Philcox, M. M. Ivanov, M. Simonović, and M. Zaldarriaga, Combining full-shape and BAO analyses of galaxy power spectra: A 1.6% CMB-independent constraint on H_0, J. Cosmol. Astropart. Phys. 05 (2020) 032.

[15] O. H. E. Philcox and M. M. Ivanov, BOSS DR12 full-shape cosmology: ΛCDM constraints from the large-scale galaxy power spectrum and bispectrum monopole, Phys. Rev. D **105**, 043517 (2022).

[16] A. Chudaykin, K. Dolgikh, and M. M. Ivanov, Constraints on the curvature of the Universe and dynamical dark energy from the Full-shape and BAO data, Phys. Rev. D **103**, 023507 (2021).

[17] O. H. E. Philcox, B. D. Sherwin, G. S. Farren, and E. J. Baxter, Determining the Hubble constant without the sound horizon: Measurements from galaxy surveys, Phys. Rev. D **103**, 023538 (2021).

[18] O. H. E. Philcox, G. S. Farren, B. D. Sherwin, E. J. Baxter, and D. J. Brout, Determining the Hubble constant without the sound horizon: A 3.6% constraint on H_0 from galaxy surveys, CMB lensing and supernovae, arXiv:2204.02984.

[19] G. D'Amico, J. Gleyzes, N. Kokron, D. Markovic, L. Senatore, P. Zhang, F. Beutler, and H. Gil-Marín, The cosmological analysis of the SDSS/BOSS data from the effective field theory of large-scale structure, J. Cosmol. Astropart. Phys. 05 (2020) 005.

[20] G. D'Amico, Y. Donath, L. Senatore, and P. Zhang, Limits on clustering and smooth quintessence from the EFTofLSS, arXiv:2012.07554.

[21] G. D'Amico, L. Senatore, P. Zhang, and H. Zheng, The Hubble tension in light of the full-shape analysis of large-scale structure data, J. Cosmol. Astropart. Phys. 05 (2021) 072.

[22] G. D'Amico, L. Senatore, and P. Zhang, Limits on *w*CDM from the EFTofLSS with the PyBird code, J. Cosmol. Astropart. Phys. 01 (2021) 006.

[23] T. Colas, G. D'amico, L. Senatore, P. Zhang, and F. Beutler, Efficient cosmological analysis of the SDSS/BOSS data from the effective field theory of large-scale structure, J. Cosmol. Astropart. Phys. 06 (2020) 001.

[24] D. Wadekar, M. M. Ivanov, and R. Scoccimarro, Cosmological constraints from BOSS with analytic covariance matrices, Phys. Rev. D **102**, 123521 (2020).

[25] Y. Kobayashi, T. Nishimichi, M. Takada, and H. Miyatake, Full-shape cosmology analysis of the SDSS-III BOSS galaxy power spectrum using an emulator-based halo model: A 5% determination of $\sigma 8$, Phys. Rev. D **105**, 083517 (2022).

[26] S.-F. Chen, Z. Vlah, and M. White, A new analysis of galaxy 2-point functions in the BOSS survey, including full-shape information and post-reconstruction BAO, J. Cosmol. Astropart. Phys. 02 (2022) 008.

[27] S.-F. Chen, M. White, J. DeRose, and N. Kokron, Cosmological analysis of three-dimensional BOSS galaxy clustering and planck CMB lensing cross correlations via lagrangian perturbation theory, J. Cosmol. Astropart. Phys. 07 (2022) 041.

[28] P. J. E. Peebles, *The Large-Scale Structure of the Universe*, (Princeton University Press, 1980), https://ui.adsabs.harvard.edu/abs/1980lssu.book.....P/abstract.

[29] P. J. E. Peebles and E. J. Groth, Statistical analysis of catalogs of extragalactic objects. V. Three-point correlation function for the galaxy distribution in the Zwicky catalog, Astrophys. J. **196**, 1 (1975).

[30] E. J. Groth and P. J. E. Peebles, Statistical analysis of catalogs of extragalactic objects. VII. Two- and three-point correlation functions for the high-resolution Shane-Wirtanen catalog of galaxies, Astrophys. J. **217**, 385 (1977).

[31] H. A. Feldman, J. A. Frieman, J. N. Fry, and R. Scoccimarro, Constraints On Galaxy Bias, Matter Density, and Primordial Non-Gausianity from the PSCz Galaxy Redshift Survey, Phys. Rev. Lett. **86**, 1434 (2001).

[32] F. A. Marin *et al.* (WiggleZ Collaboration), The WiggleZ dark energy survey: Constraining galaxy bias and cosmic growth with 3-point correlation functions, Mon. Not. R. Astron. Soc. **432**, 2654 (2013).

[33] R. Scoccimarro, H. A. Feldman, J. N. Fry, and J. A. Frieman, The bispectrum of IRAS redshift catalogs, Astrophys. J. **546**, 652 (2001).

[34] R. Scoccimarro, S. Colombi, J. N. Fry, J. A. Frieman, E. Hivon, and A. Melott, Nonlinear evolution of the bispectrum of cosmological perturbations, Astrophys. J. **496**, 586 (1998).

[35] E. Sefusatti, M. Crocce, S. Pueblas, and R. Scoccimarro, Cosmology and the bispectrum, Phys. Rev. D **74**, 023522 (2006).

[36] R. Scoccimarro, The bispectrum: From theory to observations, Astrophys. J. **544**, 597 (2000).

[37] R. Scoccimarro, H. M. P. Couchman, and J. A. Frieman, The bispectrum as a signature of gravitational instability in redshift-space, Astrophys. J. **517**, 531 (1999).
[38] H. Gil-Marín, L. Verde, J. Noreña, A. J. Cuesta, L. Samushia, W. J. Percival, C. Wagner, M. Manera, and D. P. Schneider, The power spectrum and bispectrum of SDSS DR11 BOSS galaxies—II. Cosmological interpretation, Mon. Not. R. Astron. Soc. **452**, 1914 (2015).
[39] H. Gil-Marín, J. Noreña, L. Verde, W. J. Percival, C. Wagner, M. Manera, M. Manera, and D. P. Schneider, The power spectrum and bispectrum of SDSS DR11 BOSS galaxies—I. Bias and gravity, Mon. Not. R. Astron. Soc. **451**, 539 (2015).
[40] H. Gil-Marín, W. J. Percival, L. Verde, J. R. Brownstein, C.-H. Chuang, F.-S. Kitaura, S. A. Rodríguez-Torres, and M. D. Olmstead, The clustering of galaxies in the SDSS-III baryon oscillation spectroscopic survey: RSD measurement from the power spectrum and bispectrum of the DR12 BOSS galaxies, Mon. Not. R. Astron. Soc. **465**, 1757 (2017).
[41] R. Scoccimarro, Fast estimators for redshift-space clustering, Phys. Rev. D **92**, 083532 (2015).
[42] O. H. E. Philcox and D. J. Eisenstein, Computing the small-scale galaxy power spectrum and bispectrum in configuration-space, Mon. Not. R. Astron. Soc. **492**, 1214 (2020).
[43] O. H. E. Philcox, A faster Fourier transform? Computing small-scale power spectra and bispectra for cosmological simulations in $\mathcal{O}(N^2)$ time, Mon. Not. R. Astron. Soc. **501**, 4004 (2021).
[44] T. Baldauf, M. Mirbabayi, M. Simonović, and M. Zaldarriaga, LSS constraints with controlled theoretical uncertainties, arXiv:1602.00674.
[45] C. Hahn, F. Villaescusa-Navarro, E. Castorina, and R. Scoccimarro, Constraining M_ν with the bispectrum. Part I. Breaking parameter degeneracies, J. Cosmol. Astropart. Phys. 03 (2020) 040.
[46] Y. Welling, D. van der Woude, and E. Pajer, Lifting primordial non-gaussianity above the noise, J. Cosmol. Astropart. Phys. 08 (2016) 044.
[47] A. Moradinezhad Dizgah, H. Lee, J. B. Muñoz, and C. Dvorkin, Galaxy bispectrum from massive spinning particles, J. Cosmol. Astropart. Phys. 05 (2018) 013.
[48] C. Hahn and F. Villaescusa-Navarro, Constraining M_ν with the bispectrum. Part II. The information content of the galaxy bispectrum monopole, J. Cosmol. Astropart. Phys. 04 (2021) 029.
[49] A. Moradinezhad Dizgah, M. Biagetti, E. Sefusatti, V. Desjacques, and J. Noreña, Primordial non-gaussianity from biased tracers: Likelihood analysis of real-space power spectrum and bispectrum, J. Cosmol. Astropart. Phys. 05 (2021) 015.
[50] R. Ruggeri, E. Castorina, C. Carbone, and E. Sefusatti, DEMNUni: Massive neutrinos and the bispectrum of large scale structures, J. Cosmol. Astropart. Phys. 03 (2018) 003.
[51] Y.-S. Song, A. Taruya, and A. Oka, Cosmology with anisotropic galaxy clustering from the combination of power spectrum and bispectrum, J. Cosmol. Astropart. Phys. 08 (2015) 007.
[52] D. Karagiannis, A. Lazanu, M. Liguori, A. Raccanelli, N. Bartolo, and L. Verde, Constraining primordial non-Gaussianity with bispectrum and power spectrum from upcoming optical and radio surveys, Mon. Not. R. Astron. Soc. **478**, 1341 (2018).
[53] M. Peloso and M. Pietroni, Galilean invariance and the consistency relation for the nonlinear squeezed bispectrum of large scale structure, J. Cosmol. Astropart. Phys. 05 (2013) 031.
[54] A. Kehagias and A. Riotto, Symmetries and consistency relations in the large scale structure of the universe, Nucl. Phys. **B873**, 514 (2013).
[55] P. Valageas, Kinematic consistency relations of large-scale structures, Phys. Rev. D **89**, 083534 (2014).
[56] P. Creminelli, J. Noreña, M. Simonović, and F. Vernizzi, Single-field consistency relations of large scale structure, J. Cosmol. Astropart. Phys. 12 (2013) 025.
[57] P. Creminelli, J. Gleyzes, M. Simonović, and F. Vernizzi, Single-field consistency relations of large scale structure. Part II: Resummation and redshift space, J. Cosmol. Astropart. Phys. 02 (2014) 051.
[58] P. Creminelli, J. Gleyzes, L. Hui, M. Simonović, and F. Vernizzi, Single-field consistency relations of large scale structure. Part III: Test of the equivalence principle, J. Cosmol. Astropart. Phys. 06 (2014) 009.
[59] M. Lewandowski, Violation of the consistency relations for large-scale structure with dark energy, J. Cosmol. Astropart. Phys. 08 (2020) 044.
[60] V. Yankelevich and C. Porciani, Cosmological information in the redshift-space bispectrum, Mon. Not. R. Astron. Soc. **483**, 2078 (2019).
[61] M. Crisostomi, M. Lewandowski, and F. Vernizzi, Consistency relations for large-scale structure in modified gravity and the matter bispectrum, Phys. Rev. D **101**, 123501 (2020).
[62] A. Oddo, E. Sefusatti, C. Porciani, P. Monaco, and A. G. Sánchez, Toward a robust inference method for the galaxy bispectrum: Likelihood function and model selection, J. Cosmol. Astropart. Phys. 03 (2020) 056.
[63] A. Oddo, F. Rizzo, E. Sefusatti, C. Porciani, and P. Monaco, Cosmological parameters from the likelihood analysis of the galaxy power spectrum and bispectrum in real space, J. Cosmol. Astropart. Phys. 11 (2021) 038.
[64] A. Chudaykin and M. M. Ivanov, Measuring neutrino masses with large-scale structure: Euclid forecast with controlled theoretical error, J. Cosmol. Astropart. Phys. 11 (2019) 034.
[65] F. Rizzo, C. Moretti, K. Pardede, A. Eggemeier, A. Oddo, E. Sefusatti *et al.*, The halo bispectrum multipoles in redshift space, arXiv:2204.13628.
[66] T. Baldauf, L. Mercolli, M. Mirbabayi, and E. Pajer, The bispectrum in the effective field theory of large scale structure, J. Cosmol. Astropart. Phys. 05 (2015) 007.
[67] R. E. Angulo, S. Foreman, M. Schmittfull, and L. Senatore, The one-loop matter bispectrum in the effective field theory of large scale structures, J. Cosmol. Astropart. Phys. 10 (2015) 039.
[68] A. Lazanu and M. Liguori, The two and three-loop matter bispectrum in perturbation theories, J. Cosmol. Astropart. Phys. 04 (2018) 055.

[69] D. Alkhanishvili, C. Porciani, E. Sefusatti, M. Biagetti, A. Lazanu, A. Oddo, and V. Yankelevich, The reach of next-to-leading-order perturbation theory for the matter bispectrum, Mon. Not. R. Astron. Soc. **512**, 4961 (2022).

[70] E. Sefusatti, M. Crocce, and V. Desjacques, The matter bispectrum in N-body simulations with non-Gaussian initial conditions, Mon. Not. R. Astron. Soc. **406**, 1014 (2010).

[71] P. Valageas and T. Nishimichi, Combining perturbation theories with halo models for the matter bispectrum, Astron. Astrophys. **532**, A4 (2011).

[72] R. Takahashi, T. Nishimichi, T. Namikawa, A. Taruya, I. Kayo, K. Osato, Y. Kobayashi, and M. Shirasaki, Fitting the nonlinear matter bispectrum by the halofit approach, Astrophys. J. **895**, 113 (2020).

[73] R. de Belsunce and L. Senatore, Tree-Level bispectrum in the effective field theory of large-scale structure extended to massive neutrinos, J. Cosmol. Astropart. Phys. 02 (2019) 038.

[74] E. Di Dio, R. Durrer, R. Maartens, F. Montanari, and O. Umeh, The full-sky angular bispectrum in redshift space, J. Cosmol. Astropart. Phys. 04 (2019) 053.

[75] H. Gil-Marín, C. Wagner, J. Noreña, L. Verde, and W. Percival, Dark matter and halo bispectrum in redshift space: Theory and applications, J. Cosmol. Astropart. Phys. 12 (2014) 029.

[76] V. Desjacques, D. Jeong, and F. Schmidt, The galaxy power spectrum and bispectrum in redshift space, J. Cosmol. Astropart. Phys. 12 (2018) 035.

[77] R. E. Smith, R. K. Sheth, and R. Scoccimarro, An analytic model for the bispectrum of galaxies in redshift space, Phys. Rev. D **78**, 023523 (2008).

[78] E. O. Nadler, A. Perko, and L. Senatore, On the bispectra of very massive tracers in the effective field theory of large-scale structure, J. Cosmol. Astropart. Phys. 02 (2018) 058.

[79] A. Eggemeier, R. Scoccimarro, and R. E. Smith, Bias loop corrections to the galaxy bispectrum, Phys. Rev. D **99**, 123514 (2019).

[80] M. M. Ivanov, O. H. E. Philcox, T. Nishimichi, M. Simonović, M. Takada, and M. Zaldarriaga, Precision analysis of the redshift-space galaxy bispectrum, Phys. Rev. D **105**, 063512 (2022).

[81] A. Eggemeier, R. Scoccimarro, R. E. Smith, M. Crocce, A. Pezzotta, and A. G. Sánchez, Testing one-loop galaxy bias: Joint analysis of power spectrum and bispectrum, Phys. Rev. D **103**, 123550 (2021).

[82] J. J. M. Carrasco, M. P. Hertzberg, and L. Senatore, The effective field theory of cosmological large scale structures, J. High Energy Phys. 09 (2012) 082.

[83] D. Baumann, A. Nicolis, L. Senatore, and M. Zaldarriaga, Cosmological non-linearities as an effective fluid, J. Cosmol. Astropart. Phys. 07 (2012) 051.

[84] G. Cabass, M. M. Ivanov, M. Lewandowski, M. Mirbabayi, and M. Simonović, Snowmass white paper: Effective field theories in cosmology, arXiv:2203.08232.

[85] T. Steele and T. Baldauf, Precise calibration of the one-loop bispectrum in the effective field theory of large scale structure, Phys. Rev. D **103**, 023520 (2021).

[86] M. M. Ivanov and S. Sibiryakov, Infrared resummation for biased tracers in redshift space, J. Cosmol. Astropart. Phys. 07 (2018) 053.

[87] D. Blas, M. Garny, M. M. Ivanov, and S. Sibiryakov, Time-sliced perturbation theory II: Baryon acoustic oscillations and infrared resummation, J. Cosmol. Astropart. Phys. 07 (2016) 028.

[88] L. Senatore and G. Trevisan, On the IR-resummation in the EFTofLSS, J. Cosmol. Astropart. Phys. 05 (2018) 019.

[89] M. Lewandowski and L. Senatore, An analytic implementation of the IR-resummation for the BAO peak, J. Cosmol. Astropart. Phys. 03 (2020) 018.

[90] L. Senatore and M. Zaldarriaga, The IR-resummed effective field theory of large scale structures, J. Cosmol. Astropart. Phys. 02 (2015) 013.

[91] A. Vasudevan, M. M. Ivanov, S. Sibiryakov, and J. Lesgourgues, Time-sliced perturbation theory with primordial non-Gaussianity and effects of large bulk flows on inflationary oscillating features, J. Cosmol. Astropart. Phys. 09 (2019) 037.

[92] T. Baldauf, M. Mirbabayi, M. Simonović, and M. Zaldarriaga, Equivalence principle and the baryon acoustic peak, Phys. Rev. D **92**, 043514 (2015).

[93] Z. Vlah, U. Seljak, M. Y. Chu, and Y. Feng, Perturbation theory, effective field theory, and oscillations in the power spectrum, J. Cosmol. Astropart. Phys. 03 (2016) 057.

[94] O. H. E. Philcox, Cosmology without window functions: Cubic estimators for the galaxy bispectrum, Phys. Rev. D **104**, 123529 (2021).

[95] K. Pardede, F. Rizzo, M. Biagetti, E. Castorina, E. Sefusatti, and P. Monaco, Bispectrum-window convolution via Hankel transform, arXiv:2203.04174.

[96] G. Cabass, M. M. Ivanov, O. H. E. Philcox, M. Simonović, and M. Zaldarriaga, Constraints on Single-Field Inflation from the BOSS Galaxy Survey, Phys. Rev. Lett. **129**, 021301 (2022).

[97] G. Cabass, M. M. Ivanov, O. H. E. Philcox, M. Simonović, and M. Zaldarriaga, Constraints on multi-field inflation from the BOSS galaxy survey, Phys. Rev. D **106**, 043506 (2022).

[98] G. D'Amico, M. Lewandowski, L. Senatore, and P. Zhang, Limits on primordial non-Gaussianities from BOSS galaxy-clustering data, arXiv:2201.11518.

[99] M. Simonović, T. Baldauf, M. Zaldarriaga, J. J. Carrasco, and J. A. Kollmeier, Cosmological perturbation theory using the FFTLog: Formalism and connection to QFT loop integrals, J. Cosmol. Astropart. Phys. 04 (2018) 030.

[100] T. Nishimichi, G. D'Amico, M. M. Ivanov, L. Senatore, M. Simonović, M. Takada, M. Zaldarriaga, and P. Zhang, Blinded challenge for precision cosmology with large-scale structure: results from effective field theory for the redshift-space galaxy power spectrum, Phys. Rev. D **102**, 123541 (2020).

[101] D. Gualdi and L. Verde, Galaxy redshift-space bispectrum: The importance of being anisotropic, J. Cosmol. Astropart. Phys. 06 (2020) 041.

[102] O. H. E. Philcox, J. Hou, and Z. Slepian, A first detection of the connected 4-point correlation function of galaxies using the BOSS CMASS sample, arXiv:2108.01670.

[103] D. Gualdi and L. Verde, Integrated trispectrum detection from BOSS DR12 NGC CMASS, arXiv:2201.06932.
[104] A. Eggemeier, R. Scoccimarro, M. Crocce, A. Pezzotta, and A. G. Sánchez, Testing one-loop galaxy bias: Power spectrum, Phys. Rev. D **102**, 103530 (2020).
[105] F. Bernardeau, S. Colombi, E. Gaztanaga, and R. Scoccimarro, Large scale structure of the universe and cosmological perturbation theory, Phys. Rep. **367**, 1 (2002).
[106] P. McDonald and A. Roy, Clustering of dark matter tracers: Generalizing bias for the coming era of precision LSS, J. Cosmol. Astropart. Phys. 08 (2009) 020.
[107] V. Assassi, D. Baumann, D. Green, and M. Zaldarriaga, Renormalized halo bias, J. Cosmol. Astropart. Phys. 08 (2014) 056.
[108] R. Angulo, M. Fasiello, L. Senatore, and Z. Vlah, On the statistics of biased tracers in the effective field theory of large scale structures, J. Cosmol. Astropart. Phys. 09 (2015) 029.
[109] L. Senatore, Bias in the effective field theory of large scale structures, J. Cosmol. Astropart. Phys. 11 (2015) 007.
[110] M. Mirbabayi, F. Schmidt, and M. Zaldarriaga, Biased tracers and time evolution, J. Cosmol. Astropart. Phys. 07 (2015) 030.
[111] V. Desjacques, D. Jeong, and F. Schmidt, Large-scale galaxy bias, Phys. Rep. **733**, 1 (2018).
[112] N. Kaiser, Clustering in real space and in redshift space, Mon. Not. R. Astron. Soc. **227**, 1 (1987).
[113] A. Chudaykin, M. M. Ivanov, O. H. E. Philcox, and M. Simonović, Nonlinear perturbation theory extension of the Boltzmann code CLASS, Phys. Rev. D **102**, 063533 (2020).
[114] A. Chudaykin, M. M. Ivanov, and M. Simonović, Optimizing large-scale structure data analysis with the theoretical error likelihood, Phys. Rev. D **103**, 043525 (2021).
[115] C. Alcock and B. Paczynski, An evolution free test for non-zero cosmological constant, Nature (London) **281**, 358 (1979).
[116] R. Casas-Miranda, H. J. Mo, R. K. Sheth, and G. Boerner, On the distribution of haloes, galaxies and mass, Mon. Not. R. Astron. Soc. **333**, 730 (2002).
[117] T. Baldauf, U. Seljak, R. E. Smith, N. Hamaus, and V. Desjacques, Halo stochasticity from exclusion and nonlinear clustering, Phys. Rev. D **88**, 083507 (2013).
[118] T. Baldauf, S. Codis, V. Desjacques, and C. Pichon, Peak exclusion, stochasticity and convergence of perturbative bias expansions in $1+1$ gravity, Mon. Not. R. Astron. Soc. **456**, 3985 (2016).
[119] M. Schmittfull, M. Simonović, V. Assassi, and M. Zaldarriaga, Modeling biased tracers at the field level, Phys. Rev. D **100**, 043514 (2019).
[120] D. Blas, M. Garny, M. M. Ivanov, and S. Sibiryakov, Time-sliced perturbation theory for large scale structure I: General formalism, J. Cosmol. Astropart. Phys. 07 (2016) 052.
[121] M. M. Ivanov, O. H. E. Philcox, M. Simonović, M. Zaldarriaga, T. Nischimichi, and M. Takada, Cosmological constraints without nonlinear redshift-space distortions, Phys. Rev. D **105**, 043531 (2022).
[122] O. H. E. Philcox, M. M. Ivanov, M. Zaldarriaga, M. Simonovic, and M. Schmittfull, Fewer mocks and less noise: Reducing the dimensionality of cosmological observables with subspace projections, Phys. Rev. D **103**, 043508 (2021).
[123] J. C. Jackson, Fingers of God: A critique of Rees' theory of primordial gravitational radiation, Mon. Not. R. Astron. Soc. **156**, 1P (1972).
[124] A. Barreira, The squeezed matter bispectrum covariance with responses, J. Cosmol. Astropart. Phys. 03 (2019) 008.
[125] A. Barreira, On the impact of galaxy bias uncertainties on primordial non-Gaussianity constraints, J. Cosmol. Astropart. Phys. 12 (2020) 031.
[126] M. Biagetti, L. Castiblanco, J. Noreña, and E. Sefusatti, The covariance of squeezed bispectrum configurations, arXiv:2111.05887.
[127] B. Audren, J. Lesgourgues, S. Bird, M. G. Haehnelt, and M. Viel, Neutrino masses and cosmological parameters from a Euclid-like survey: Markov Chain Monte Carlo forecasts including theoretical errors, J. Cosmol. Astropart. Phys. 01 (2013) 026.
[128] T. Brinckmann and J. Lesgourgues, MontePython 3: Boosted MCMC sampler and other features, Phys. Dark Universe **24**, 100260 (2019).
[129] V. Assassi, D. Baumann, E. Pajer, Y. Welling, and D. van der Woude, Effective theory of large-scale structure with primordial non-Gaussianity, J. Cosmol. Astropart. Phys. 11 (2015) 024.
[130] D. Bertolini, K. Schutz, M. P. Solon, and K. M. Zurek, The trispectrum in the effective field theory of large scale structure, J. Cosmol. Astropart. Phys. 06 (2016) 052.
[131] T. Baldauf, E. Schaan, and M. Zaldarriaga, On the reach of perturbative methods for dark matter density fields, J. Cosmol. Astropart. Phys. 03 (2016) 007.
[132] T. Lazeyras, C. Wagner, T. Baldauf, and F. Schmidt, Precision measurement of the local bias of dark matter halos, J. Cosmol. Astropart. Phys. 02 (2016) 018.
[133] M. M. Abidi and T. Baldauf, Cubic halo bias in Eulerian and Lagrangian space, J. Cosmol. Astropart. Phys. 07 (2018) 029.
[134] F. Schmidt, G. Cabass, J. Jasche, and G. Lavaux, Unbiased cosmology inference from biased tracers using the EFT likelihood, J. Cosmol. Astropart. Phys. 11 (2020) 008.
[135] M. Schmittfull, M. Simonović, M. M. Ivanov, O. H. E. Philcox, and M. Zaldarriaga, Modeling galaxies in redshift space at the field level, J. Cosmol. Astropart. Phys. 05 (2021) 059.
[136] T. Lazeyras, A. Barreira, and F. Schmidt, Assembly bias in quadratic bias parameters of dark matter halos from forward modeling, J. Cosmol. Astropart. Phys. 10 (2021) 063.
[137] A. Barreira, T. Lazeyras, and F. Schmidt, Galaxy bias from forward models: linear and second-order bias of IllustrisTNG galaxies, J. Cosmol. Astropart. Phys. 08 (2021) 029.

[138] T. Steele and T. Baldauf, Precise calibration of the one-loop trispectrum in the effective field theory of large scale structure, Phys. Rev. D **103**, 103518 (2021).

[139] D. Blas, M. M. Ivanov, and S. Sibiryakov, Testing Lorentz invariance of dark matter, J. Cosmol. Astropart. Phys. 10 (2012) 057.

[140] B. Audren, D. Blas, M. M. Ivanov, J. Lesgourgues, and S. Sibiryakov, Cosmological constraints on deviations from Lorentz invariance in gravity and dark matter, J. Cosmol. Astropart. Phys. 03 (2015) 016.

[141] L. Senatore and M. Zaldarriaga, Redshift space distortions in the effective field theory of large scale structures, arXiv:1409.1225.

[142] M. Lewandowski, L. Senatore, F. Prada, C. Zhao, and C.-H. Chuang, EFT of large scale structures in redshift space, Phys. Rev. D **97**, 063526 (2018).

[143] A. Perko, L. Senatore, E. Jennings, and R. H. Wechsler, Biased tracers in redshift space in the EFT of large-scale structure, arXiv:1610.09321.